NASA-CR-198805

THE ONSET OF ELECTROHYDRODYNAMIC INSTABILITY IN ISOELECTRIC FOCUSING

FINAL TECHNICAL REPORT, NASA GRANT NAG8-909

submitted by

James C. Baygents, Ph.D.
Principal Investigator
Department of Chemical Engineering
THE UNIVERSITY OF ARIZONA
TUCSON, AZ 85721

PERIOD OF GRANT: 14 APRIL 1992—31 DECEMBER 1993

(NASA-CR-198805) THE ONSET OF ELECTROHYDRODYNAMIC INSTABILITY IN ISOELECTRIC FOCUSING Final Technical Report, 14 Apr. 1992 - 31 Dec. 1993 (Arizona Univ.) 79 p

N95-29968

Unclas

G3/33 0055368

SUMMARY

The onset of electrohydrodynamic motion associated with the imposition of an electric field across a thin layer of liquid has been investigated for the case in which the electrical conductivity varies linearly over the depth of the layer. The variation of the conductivity is due to concentration gradients in the charge-carrying solutes and its spatio-temporal evolution is represented by a convective-diffusion equation. When the viscous relaxation time is long compared to the time for charge relaxation, the analysis reveals that the neutral stability curves for the layer can be characterized by three dimensionless parameters: $Ra_e \equiv d\varepsilon E_0^2 \Delta\sigma/\mu K_{eff}\,\sigma_0$, an electrical Rayleigh number; $\Delta\sigma/\sigma_0$, the relative conductivity increment; and α, the transverse wave number of the disturbance. Here d is the thickness, ε is the dielectric constant, and μ is the viscosity of the layer, E_0 is the applied field strength at the lower conductivity boundary, and K_{eff} is an effective diffusivity associated with the Brownian motion of the charge-carrying solutes. With viscous-stress-free boundaries, at which the electrical conductivity and the normal component of the electric field are prescribed, the critical Ra_e is 1.504×10^4 at a critical transverse wave number of 1.98 when $\Delta\sigma/\sigma_0$ is 10. As $\Delta\sigma/\sigma_0$ increases, the critical Ra_e increases and shifts to shorter wavelength disturbances; the critical imposed field strength, however, passes through a minimum because the lower-conductivity boundary exerts a considerable stabilizing influence in the presence of steep conductivity gradients. Similar trends were obtained for liquid layers with rigid boundaries.

TABLE OF CONTENTS

CHAPTER 1 : BACKGROUND AND MOTIVATION

Background

Developments in the area of biotechnology have created the need to isolate and purify large quantities of biological materials. A common (analytical) technique used to purify small quantities of biomaterials is electrophoresis.

> Electrophoresis is the single most useful technique for the analysis and separation of proteins and nucleic acids. Its usefulness is based on its high resolution and applicability to a broad range of entities, from simple ions to living cells. It is also an inherently gentle technique, without deleterious effects on such delicate biological structures as organelles, living cells or intact chromosomes [1].

Electrophoresis is based on the principle that most biological materials in an aqueous solution are electrically charged (due to ionization) and, therefore, move under the influence of an external electric field. Biological particulates and solutes migrate at a rate that is dependent on such things as their electrical charge, their size and shape, and the properties of the solution in which they are immersed. Biomaterials for which electrophoresis may be employed include macro-ions, complex polyelectrolytes, and colloidal particles and living cells. Analytic electrophoretic separations are carried out in four classical modes: moving boundary electrophoresis (MBE), zone electrophoresis (ZE), isotachophoresis (ITP), and isoelectric focusing (IEF) [2].

With MBE, ZE and ITP, isolation and separation of species is based on differences in the electrophoretic mobility of the components—that is, on the rate of migration of the species in solution under the influence of an

external electric field. In IEF, on the other hand, the separation is based on differences in the isoelectric points of components [3]. IEF was developed to fractionate amphoteric species, molecules that act either as acids or as bases depending on the local pH of the solution. Amphoteric species typically contain both carboxyl and amine groups, so IEF is used on mixtures of peptides and/or proteins.

IEF depends on the formation of a stable pH gradient along which the components migrate until reaching their respective isoelectric points (pI). The pI of a charged species is the pH at which the net surface charge is nil [2]. An externally-applied electric field acts on the charged component and displaces it toward the region of isoelectric pH. Any movement away from this point in the pH gradient results in the ionization of the species, which causes the species to migrate back to its pI. Thus steady-state is achieved.

Though IEF is a technique tailored for the separation and characterization of amphoteric materials, when carried out in free solution, its effectiveness is diminished by fluid motion that disrupts the pH gradient. Experiments were conducted at The University of Arizona Center for Separation Science (CSS) to examine the causes of convection in IEF. The goal of The University of Arizona work was to develop ways to suppress the deleterious effects of convection so that free-solution IEF could be scaled-up to the preparative level, permitting large quantities of peptides and proteins to be processed. The CSS experiments showed that, owing to concentration gradients, buoyancy-driven convection occurred when the solutes to be separated were localized in considerable quantity—a problem

termed zone over-loading. Sedimentation occurred if the biological particulates were too large. Furthermore, imposition of an electric field caused joule heating in the electrolyte and a radial temperature gradient developed, causing natural convection. Joule heating limited the cross-sectional area of the device in which a quiescent IEF separation could be carried out to that of a capillary. Obviously such device-size limitations meant that free-solution IEF could not be done on a preparative scale unless measures were taken to either control or circumvent the problems associated with natural convection.

Subsequent investigations of IEF by the CSS (under the auspices of NASA) made use of microgravity conditions to suppress buoyancy-driven flow. The microgravity experiments uncovered still another form of convection that disrupted the focusing process. It was postulated that the convection observed in the microgravity experiments was due to electroosmotic and electrohydrodynamic effects. These electrically-driven flows, though present in the terrestrial experiments, were masked by gravitational effects.

Electroosmosis arises as a result of the electrical charge present on the surfaces of the IEF chamber. Charge on the glass vessel walls interacts with the ions in solution, and this causes a diffuse layer of charge to accumulate immediately adjacent to the chamber walls. The externally-applied electric field acts on the accumulated charge, setting the electrolyte in motion. Electrohydrodynamic effects are caused by local deviations from electroneutrality within the volume of the solution. Free volume charge accumulates due to conductivity gradients that develop during IEF.

The presence of conductivity gradients is a characteristic feature of IEF and can be understood qualitatively by recognizing that zones in which different species concentrate will conduct current at different rates. As shown in Fig. 1, quantitative descriptions of the conductivity profile in an IEF chamber are available through the use of a simulation program developed at the CSS.

One clear implication of the CSS experiments is that even if buoyancy-driven convection can be eliminated—either by use of space-based platforms, or by innovative instrument design—free-solution IEF cannot be done on the preparative scale unless electrically-driven convection is also controlled. A more subtle implication of the CSS experiments is that producing *quiescent* solutions for preparative-scale IEF may be *inherently* problematic. Indeed preparative-scale IEF instruments developed at the CSS make use of forced convection to over-ride natural and electrically-driven convection; that is, preparative-scale IEF was shown to be quite feasible if the focusing process was carried out in solutions that were made to flow by design rather than by deleterious effects.

As noted, steep electrical conductivity gradients develop along an IEF chamber as the focusing process proceeds. Detailed analysis of the flight data suggests that such conductivity gradients are the primary cause of the undesirable convection observed in the space experiments. A question that ought to be addressed, then, is the following: Suppose that a perfectly quiescent solution can be produced for the initial stages of an IEF experiment. As the conductivity gradients in the solution continue to sharpen, will the solution remain quiescent? It is the purpose here to

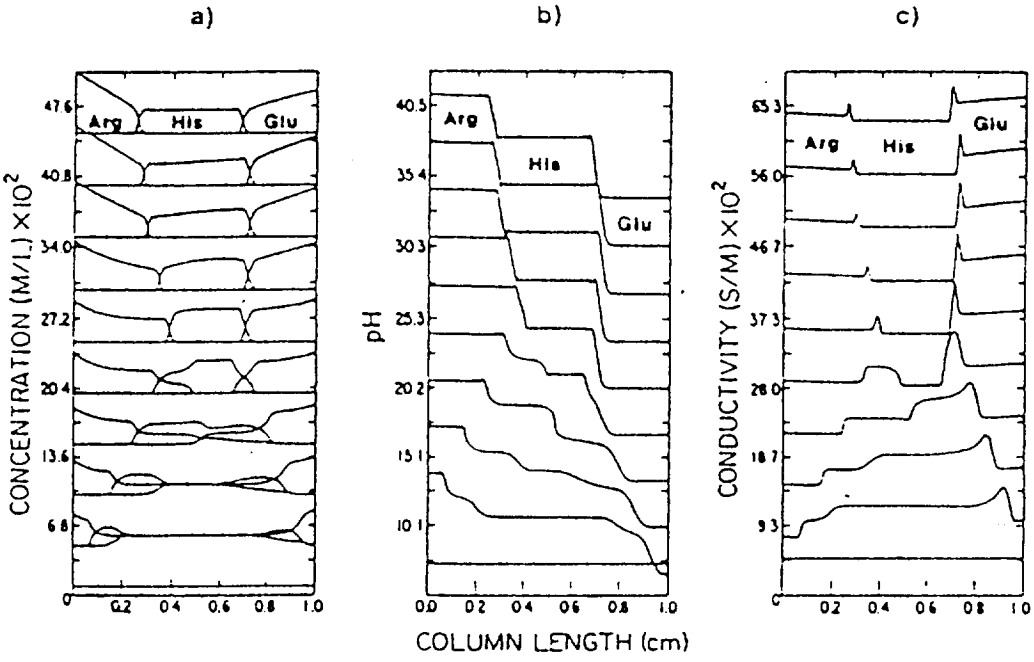

Fig. 1 Computer simulated concentration (a), pH (b) and conductivity profiles for a mixture of Arginine (Arg), Histidine (His) and Glutamic acid. Time points are, from bottom to top, 0, 5, 10, 15, 20, 50, 100, 150 and 400 min. Offset for concentration, pH and conductivity are 50 mM, 3.4 pH units and 0,07 S/m respectively [3].

Table 1
Computer Simulation

General Values

Column length	1 *cm*
Segmentation	100 segments/cm
Current density	0.001 A/cm^2

pK_a and Mobility Values

Component	pK_{a1}	pK_{a2}	Mobility x 10^4 $[cm^2/Vs]$
Glutamic acid	2.16	4.29	2.97
Histidine	6.02	9.17	2.85
Arginine	9.04	12.48	2.26
H_3O^+			36.27
OH^-			19.87

examine this very question by investigating the onset of electrohydrodynamic motion associated with sharp conductivity gradients.

For the balance of this chapter, the results of the CSS space-flight experiments will be discussed, beginning with a summary of how an IEF experiment proceeds. Next, the flight results will be recounted and, thereafter, results from computer simulations of the flight experiments will be presented. Having thus established a feel for the physico-chemical process involved in IEF, we then proceed to Chapter 2, in which an analysis of the onset of electrohydrodynamic motion is performed. Note that data and figures pertaining to the IEF space flight experiments have been reproduced from articles and technical reports written at the CSS [4].

Analysis of Space Flight Experiments

Summary Description of IEF

The general mechanism of IEF may be described with the help of Fig. 2, where the separation mechanism for a three component mixture is shown. The most basic species of the mixture is component A, the most acidic is component C, and component B has an intermediate pI.

Two separate phases may be identified during the process: a separation phase and a stabilizing phase. In the first phase, components in solution distribute in zones along the capillary separation length according to their pIs. In the second phase, the system stabilizes and reaches steady-state.

During the separation phase, two distinct transient stages are seen. Fig. 2a depicts the initial distribution of components in the separation

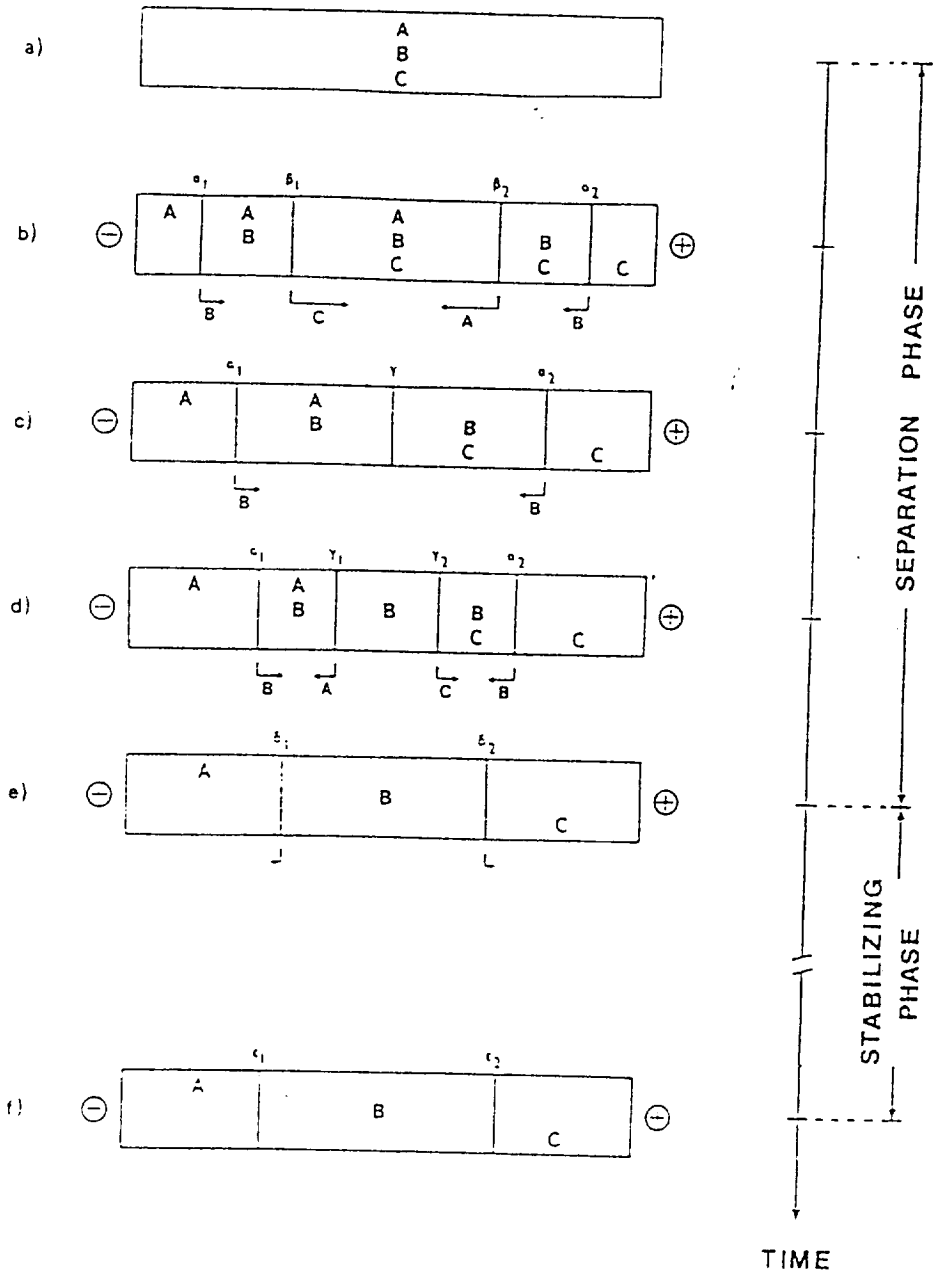

Fig. 2 Idealized representation of the stages in an IEF process.

capillary, before any external electric field is applied; note the components are distributed evenly. When the potential is applied (Fig. 2b), two moving boundaries are formed near each electrode. An α boundary appears between pure-component and mixed-component zones. Faster moving β boundaries appear between mixed component zones. The arrows beneath the boundaries indicate the direction of motion of the species; the length of the arrow specifies the relative speed of boundary movement. Thus, A and C are the fastest moving components, and they move toward opposite electrodes. In Fig. 2c, the faster β boundaries meet, and the original three component mixture has vanished. A pure B component zone then appears (Fig. 2d) and again there are four moving boundaries. The outer (α) boundaries migrate inward, reflecting motion of component B toward its pI. The inner (γ) boundaries move toward the electrodes, indicating that components A and C tend to focus at the electrodes. As α and γ boundaries meet, a three zone solution forms, with each zone comprised of a pure component (Fig. 2e). In this stage, δ boundaries form and migrate slowly toward the electrodes. This marks the end of the separation phase and the beginning of the stabilizing stage. During the interval between stage (e) and (f), the steady-state composition distribution is slowly approached. The stabilizing phase is characteristically a much slower process that the separation phase; typically the same time is required to pass from stage (a) to (e) as is then required to go from stage (e) to (f) [3].

Flight Experiments

IEF experiment were performed in microgravity conditions during two NASA missions: STS-11 and STS-26.

The first space experiment was aimed at exploring the influence of electroosmosis on IEF. Electroosmotic effects were studied by applying an anti-electroosmosis coating on the inside of the chamber walls, and by segmenting the separation chambers so as to interrupt flow along the walls. IEF chambers were built from segments of glass conduit, which were attached end to end in three ways: (1), as a simple series of cylinders; (2), as a series of tubes connected by monofilament screens; and (3), as a series of tubes with mylar constrictors set in between (i.e., baffles of rigid mylar with openings half the internal diameter of the glass segments). The five chamber types are shown in Fig. 3. The current passing through the chambers was recorded to monitor conductivity changes in the solution. Also, photographic records of the protein focusing were obtained since "red" (Hemoglobin) and "blue" (Albumin) stained species were chosen as the compounds for separation.

Plots of normalized current versus time follow in Figs. 4-9. The experimental results indicate that the columns partitioned by monofilament screens perform best. With monofilament screens the current decreases steadily as the charged species reach their pIs, and the final current is about one tenth of the initial value. The columns with mylar baffles also exhibited focusing that occurred steadily and completely. However, columns that did not contain partitions displayed a quite different behavior: a sudden increase in current followed an initial decline, and the final

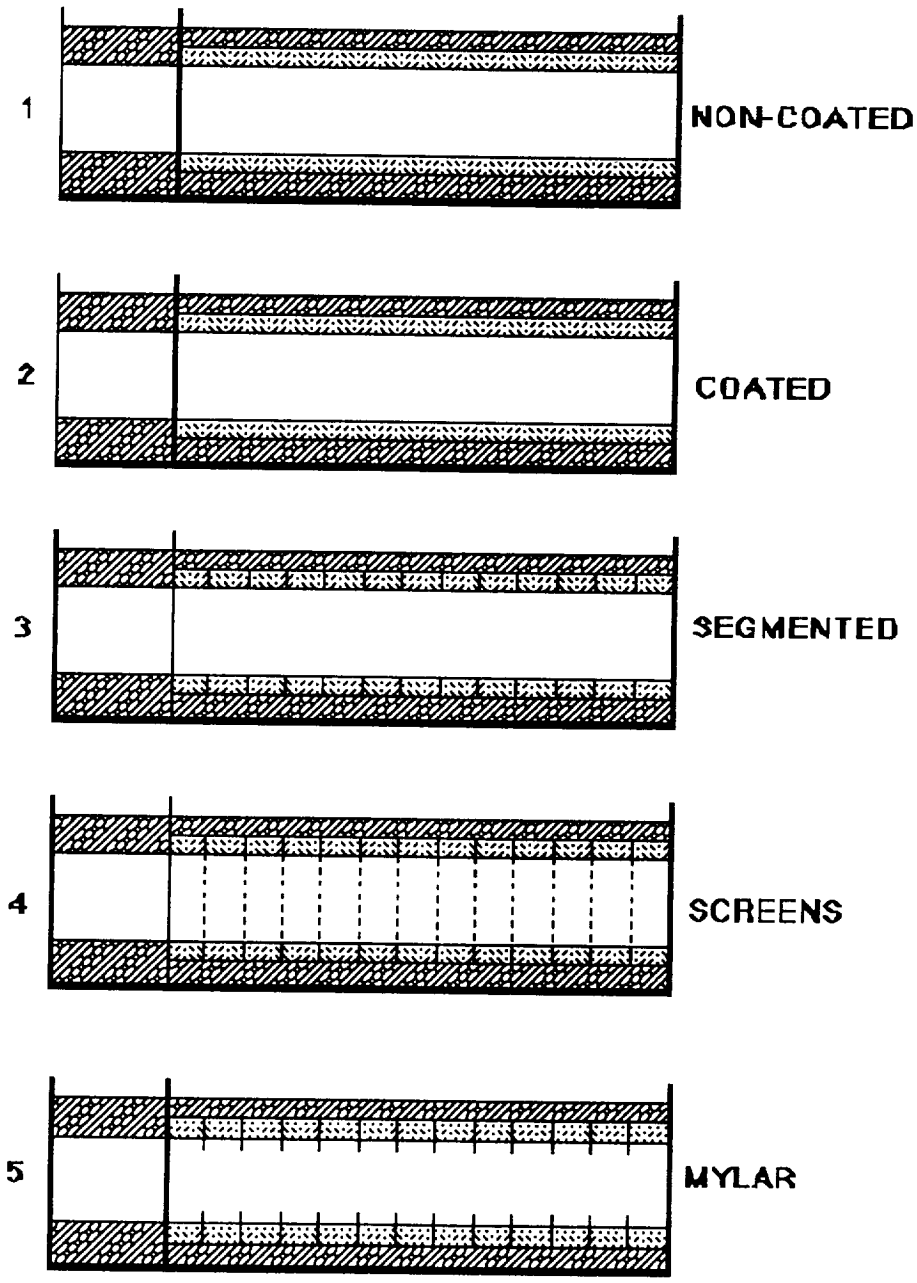

Fig. 3 Cell cross-sections for the STS-11 experiments.

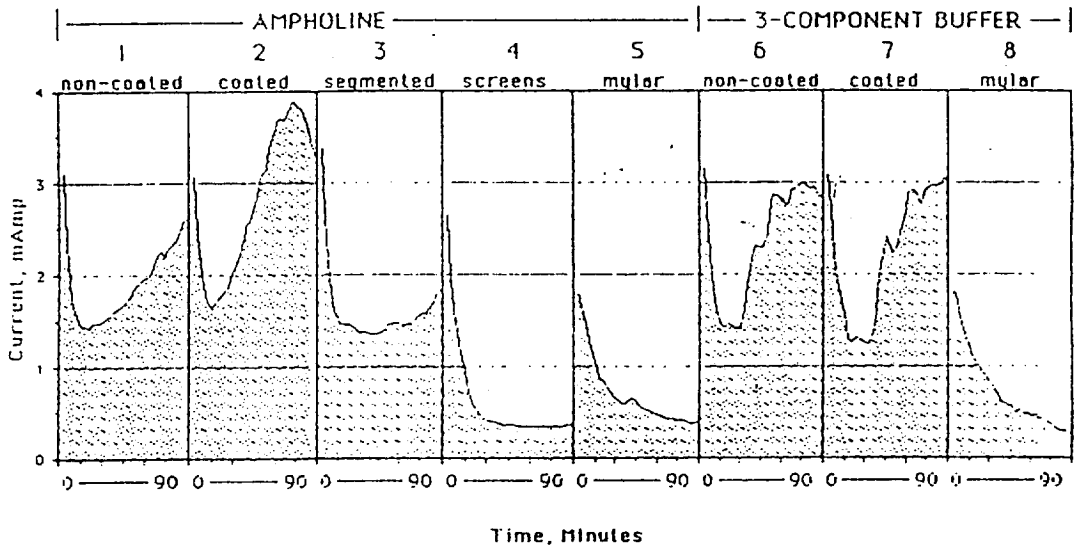

Fig. 4 Plot of current measurements versus time for the cells on the STS-11 mission.

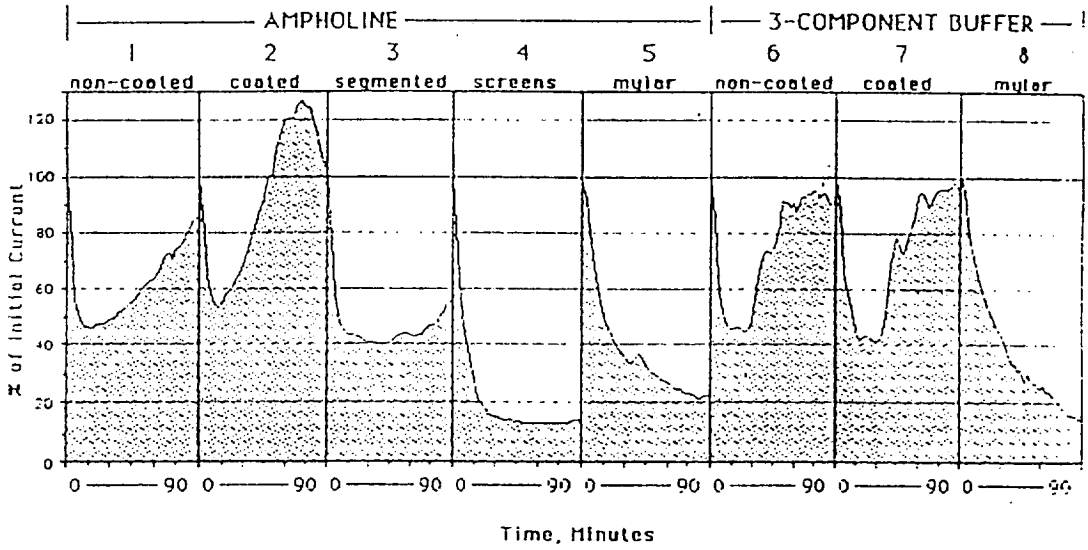

Fig. 5 Plot of normalized current measurements versus time for the cells on the STS-11 mission.

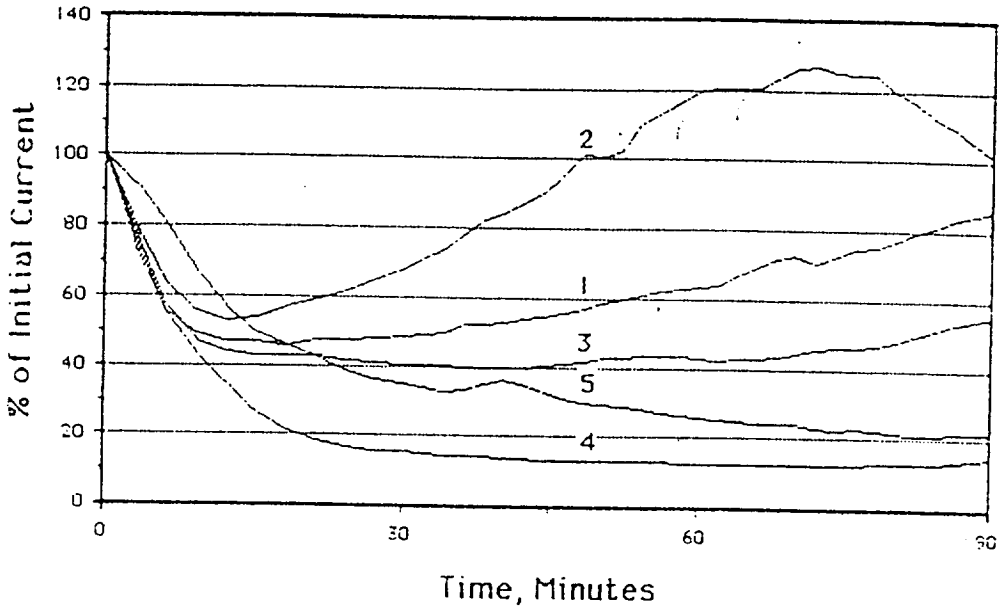

Ampholine Focusing Solutions

Cell # 2 : coated
Cell # 1 : uncoated
Cell # 3 : segmented
Cell # 5 compartmented with mylar
Cell # 4 : compartmented with screens

Fig. 6 Plot of normalized current measurements versus time for the cells containing solutions of ampholine.

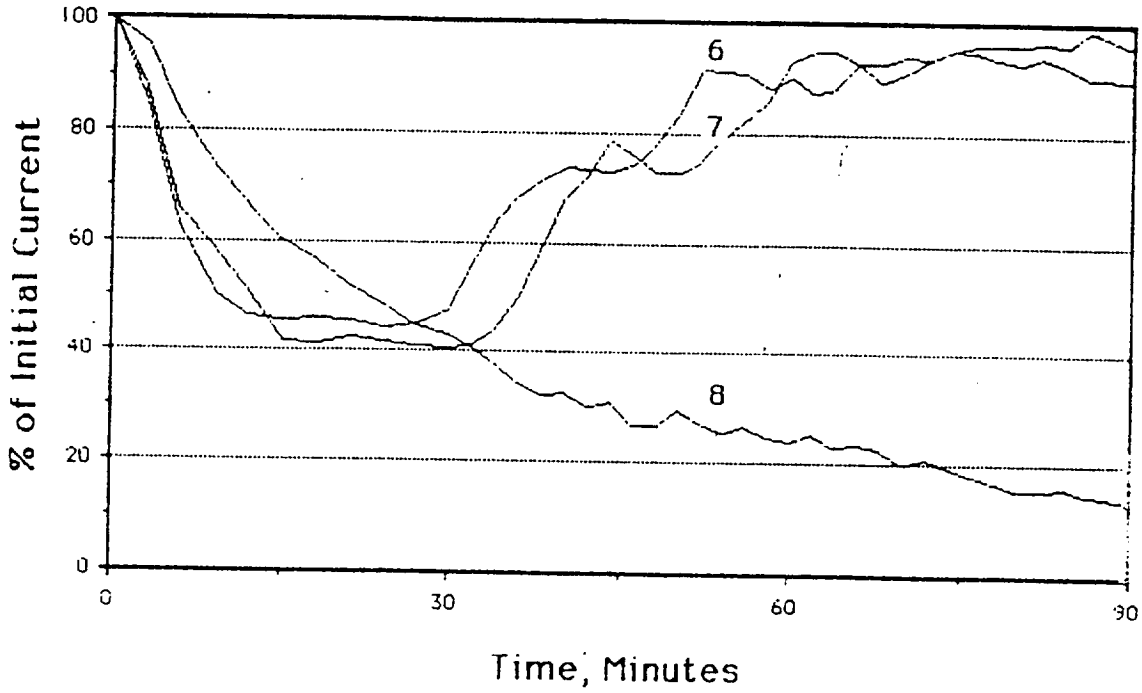

Fig. 7 Plot of normalized current measurements versus time for the cells containing solutions of 3-component buffer.

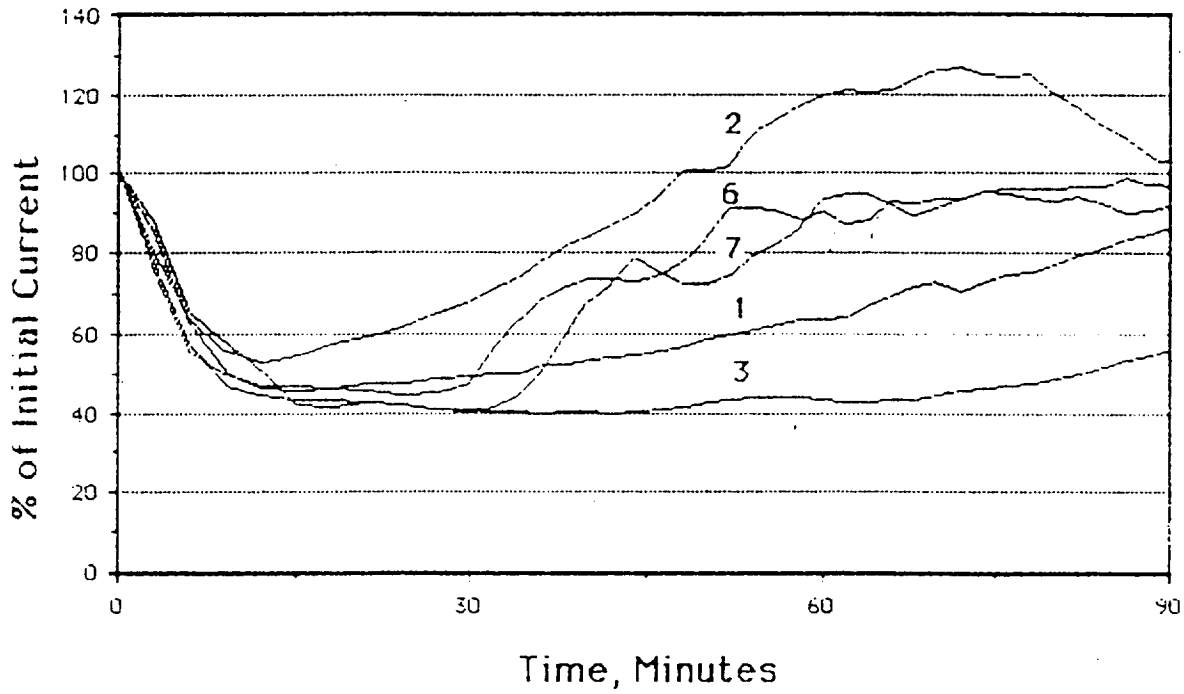

Non-Compartmented Cells

Cell # 2	Ampholine	coated
Cell # 6	3-component buffer	uncoated
Cell # 7	"	coated
Cell # 1	Ampholine	uncoated
Cell # 3	"	segmented

Fig. 8 Plot of normalized current measurements versus time for non-compartmented cells on the STS-11 mission.

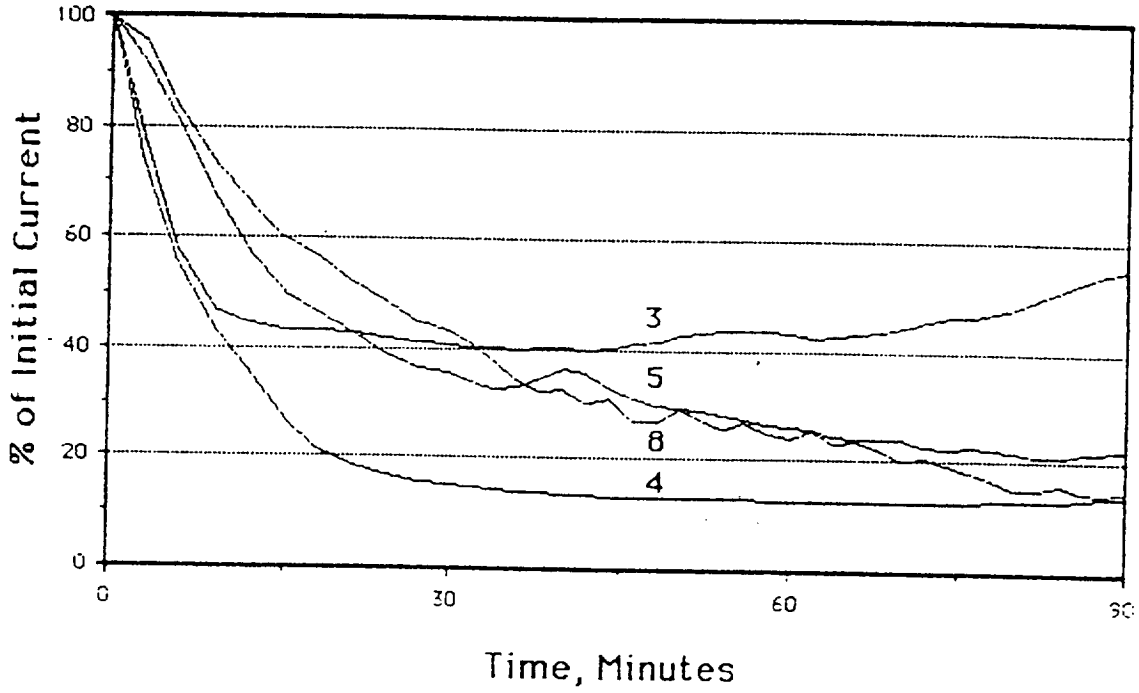

Segmented Cells

Cell # 3 :	Ampholine	segmented
Cell # 5 :	"	compartmented with mylar
Cell # 8 :	3-component buffer	" " "
Cell # 4	Ampholine	" " screens

Fig. 9 Plot of normalized current measurements versus time for segmented cells on the STS-11 mission.

current measured close to the initial value. The same occurred when anti-electroosmosis coatings were present. Since the current increases were not synchronized for these columns (Figs. 8 and 9), an external disturbance such as a sudden acceleration of the Shuttle does not explain the data. Rather the onset of electrically-driven convection within the separation chamber, causing mixing of the components, seems to be the most plausible explanation for the current increases.

Although the chambers with baffles or screens performed well, the fluid velocity observed in the unsegmented chambers was *ca.* 1 cm/min., much too strong to be attributed solely to electroosmosis. Thus, the current increases must have involved another kind of electrically-driven fluid motion, which Rhodes *et. al.* [5] subsequently deduced must be electrohydrodynamic in nature.

Another noteworthy observation was that once convection ensued, it continued throughout the experiment; a more intuitive, cyclic behavior of focusing-mixing-refocusing did not occur.

Once all elements from the STS-11 experiments and their post-flight analysis were put together, a new set of experiments was devised and flown on STS-26. The STS-26 experiments were aimed at verifying the STS-11 results, and at defining the relative magnitude of electroosmotic (EO) and electrohydrodynamic (EHD) effects. EO is a wall effect (proportional to the surface area of the IEF wall) that is proportional to the magnitude of the applied field. On the other hand, EHD is a bulk effect (proportional to the volume of the column), and it is proportional to the square of the magnitude of the applied field. Thus, varying the surface to volume ratio

of the IEF chamber at constant field strength varies the relative strength of the two flows. The chamber configurations tested on STS-26 are shown in Fig. 10. Note that cylindrical chambers were included to repeat the STS-11 experiments.

The experimental data from STS-26 are summarized in Figs. 11-16. The extent of the focusing, the time of first observable convection, and the strength of flow were comparable to the STS-11 observations for the cylindrical chambers. Screens and a larger surface to volume ratio improved the focusing performance of the columns, implying that EHD is the principal cause of the STS-11 current increases. Moreover, the performance of the rectangular cells showed a surface to volume ratio dependence.

Simulation Results

The simulation package developed at the CSS was used to estimate the magnitude of the conductivity gradients that developed during the STS-11 and STS-26 flight experiments. Refer to Table 2a for data used in the simulation.

The evolution of conductivity profile obtained is depicted in Fig. 17, and the final concentration profile in Fig. 18. The results obtained show evidence of numerical instabilities in the computer code and the simulation failed before reaching steady-state. Problems arise in the simulation because of the steep pH gradients that develop. Also, the complexity of the separation of a five component mixture adds to the numerical difficulties. In order to obtain a better estimate of the conductivity profile, it was

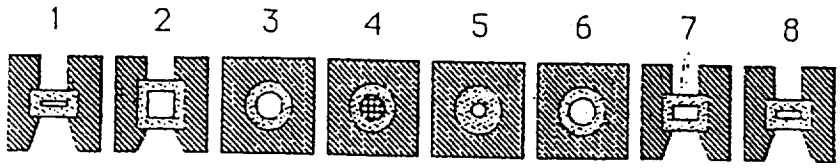

Column Number	Block	Cuvette Shape	Internal Dimensions	Buffer	Protein	Special Features
1	aluminum	rectangular	0.250 x 0.040"	3-component	Hb + Alb	none
2	-	square	0.250 x 0.240"	-	-	-
3	acrylic	round	0.250" I.D.	-	-	-
4	-	-	-	-	-	segmented
5	-	-	0.125" I.D.	-	-	none
6	-	-	0.250" I.D.	-	none	-
7	aluminum	rectangular	0.250 x 0.120"	-	Hb + Alb	-
8	-	-	0.250 x 0.060"	-	-	-

glass aluminum acrylic nylon screen

Fig. 10 Cell cross-section for the STS-26 experiments.

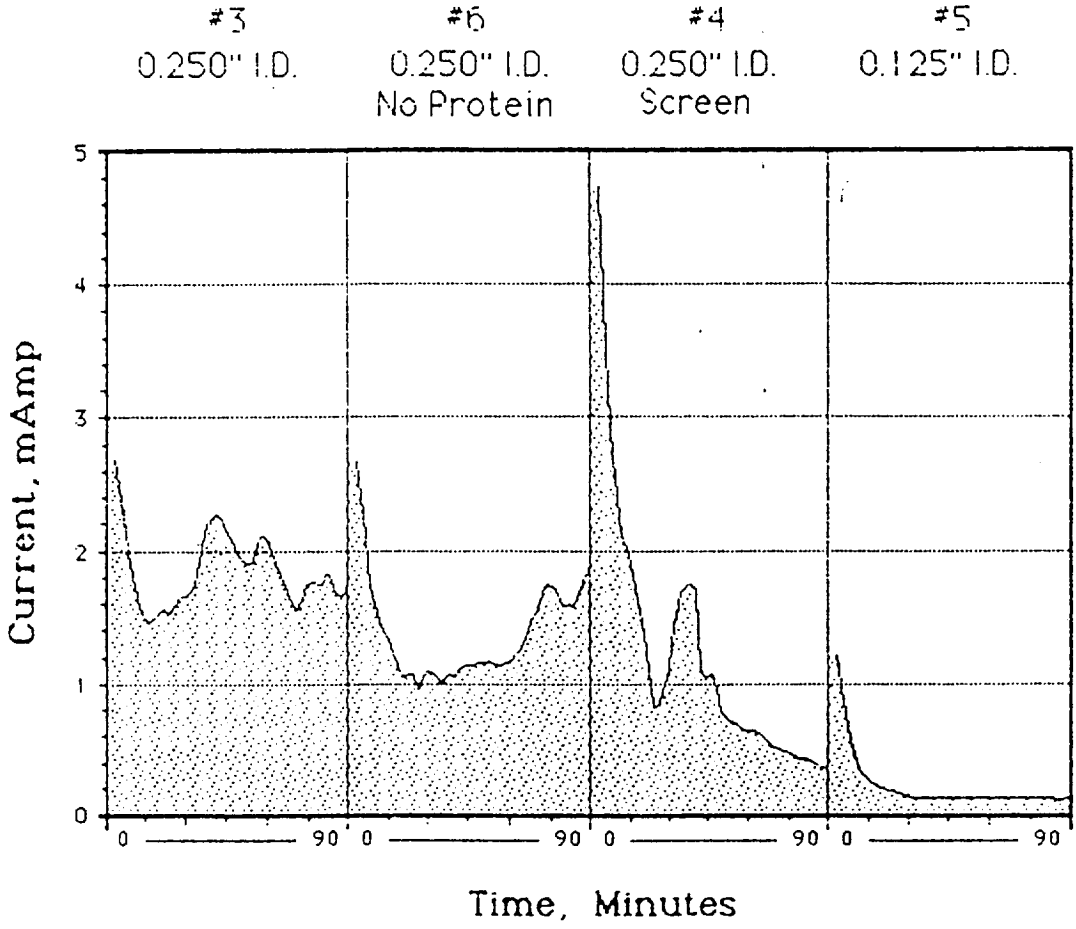

Fig. 11 Plot of current measurements versus time for cylindrical cells on the STS-26 mission.

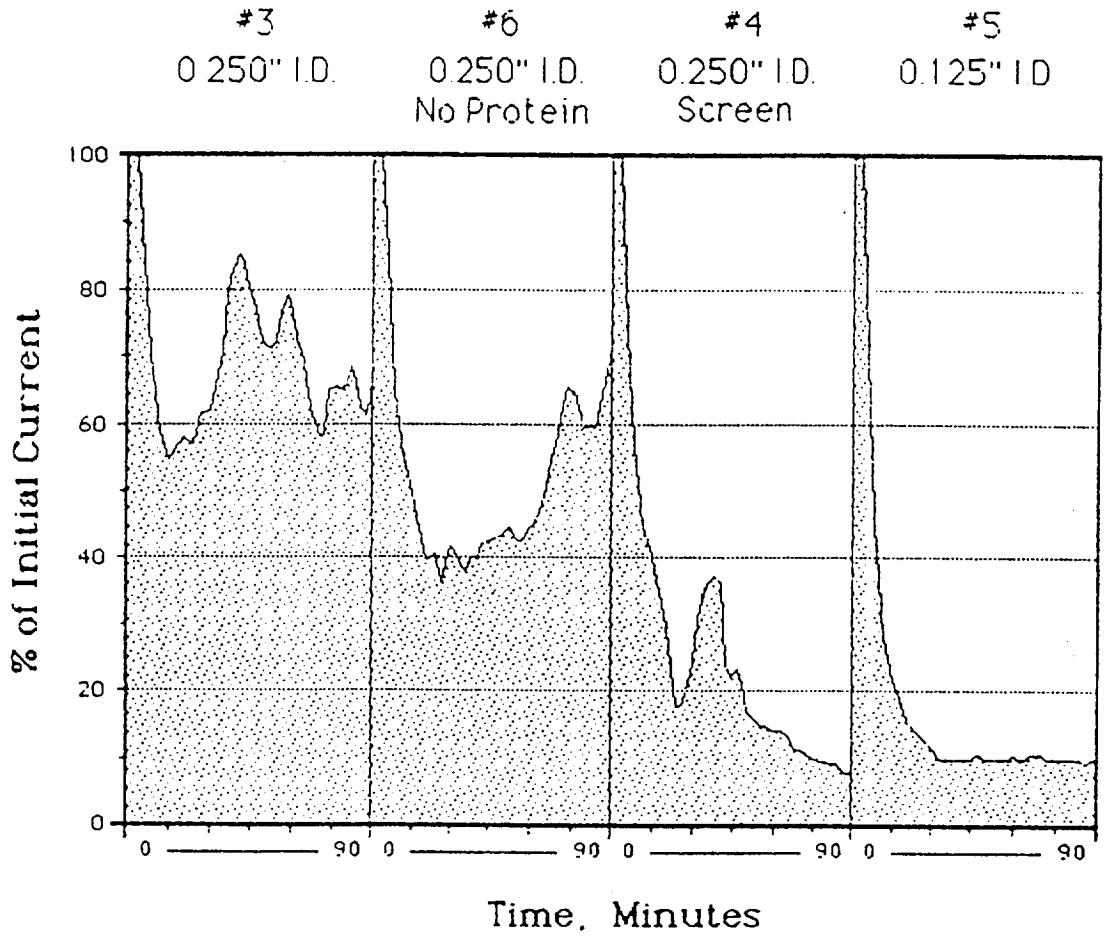

Fig. 12 Plot of normalized current measurements versus time for cylindrical cells on the STS-26 mission.

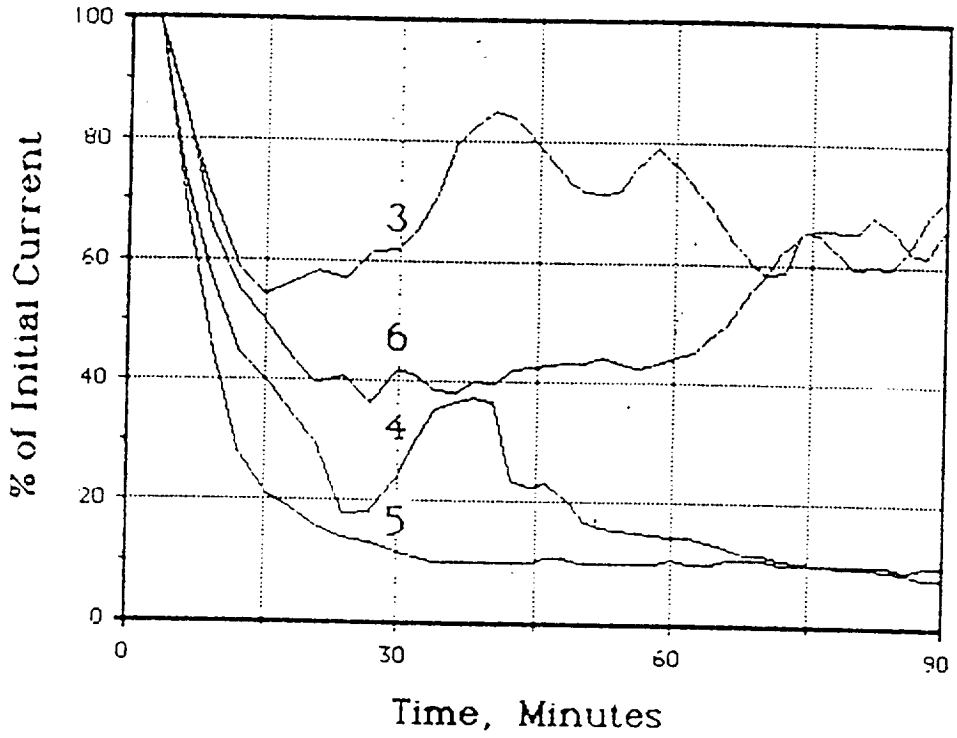

Cylindrical Cells

Cell #3: 0.250" I. D.
Cell #6: 0.250" I. D. no protein
Cell #4 0.250" I. D. screen compartmented
Cell #5: 0.125" I. D.

Fig. 13 Plot of normalized current measurements versus time for cylindrical cells on the STS-26 mission.

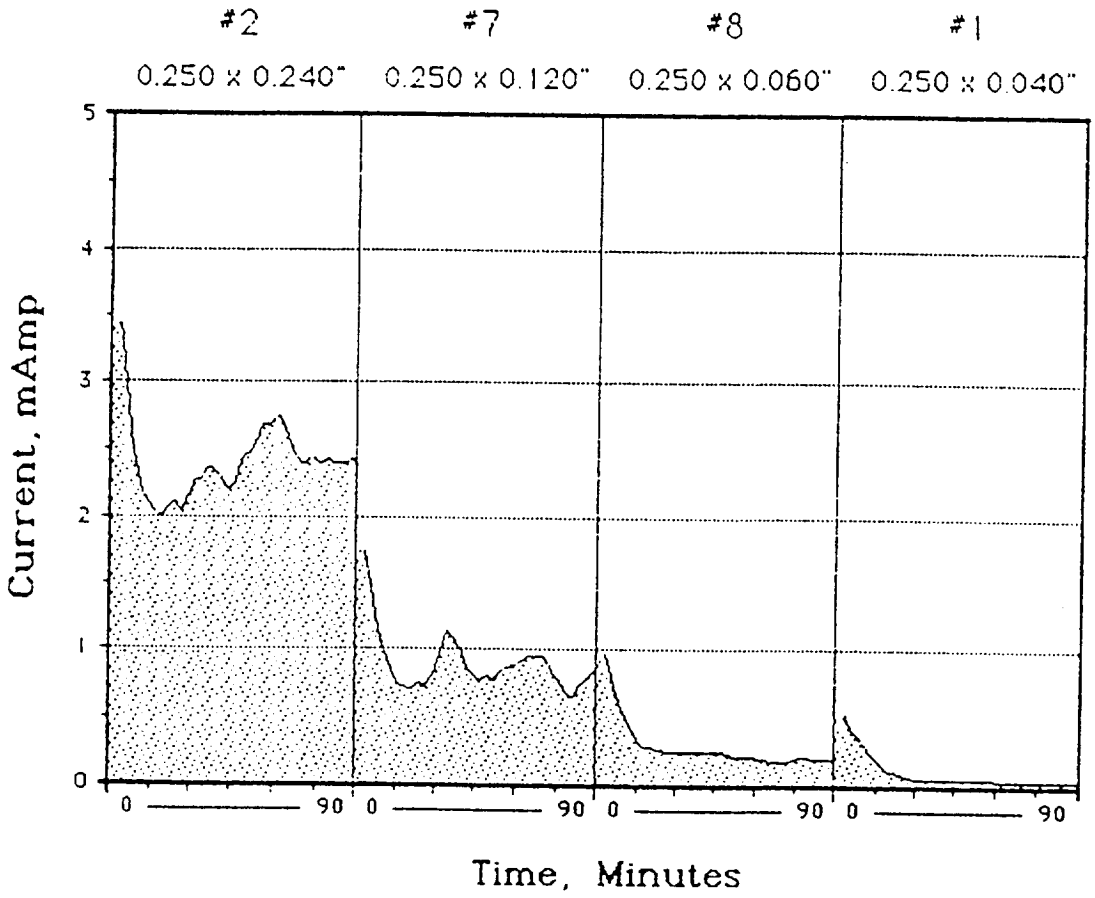

Fig. 14 Plot of current measurements versus time for rectangular cells on the STS-26 mission.

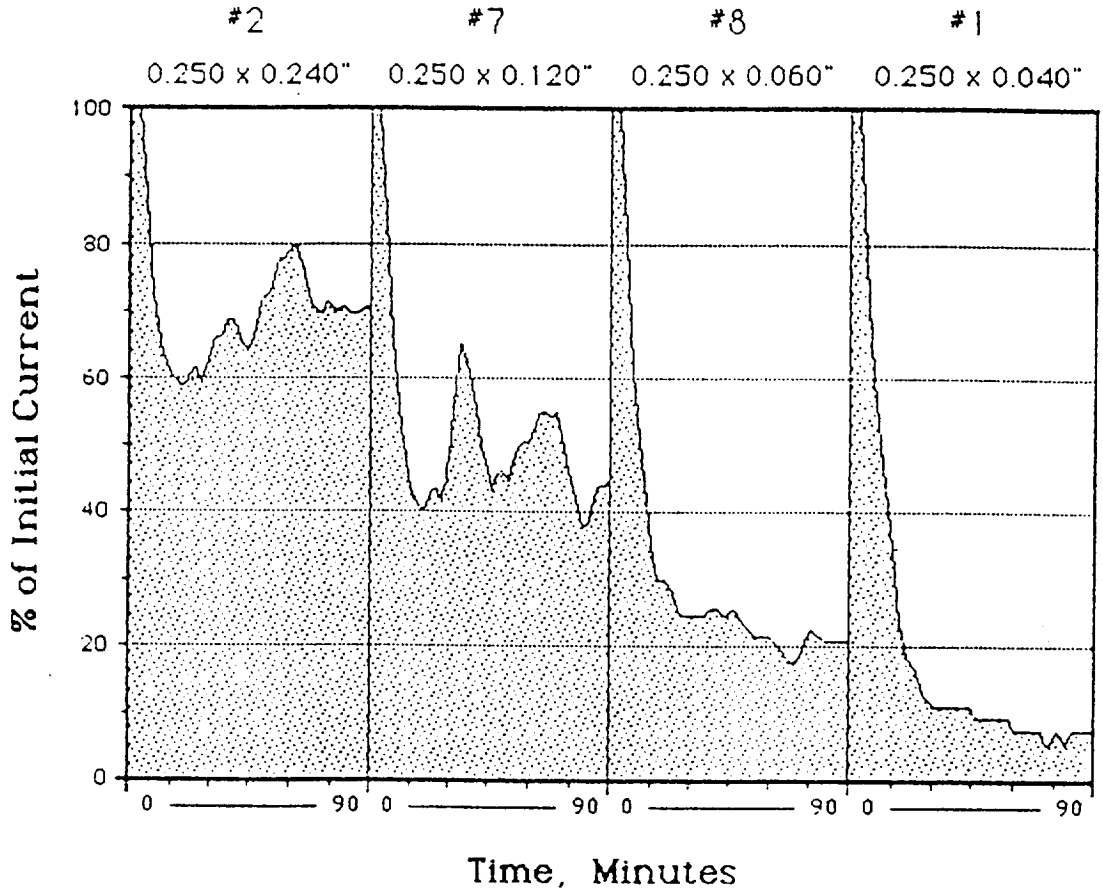

Fig. 15 Plot of normalized current measurements versus time for rectangular cells on the STS-26 mission.

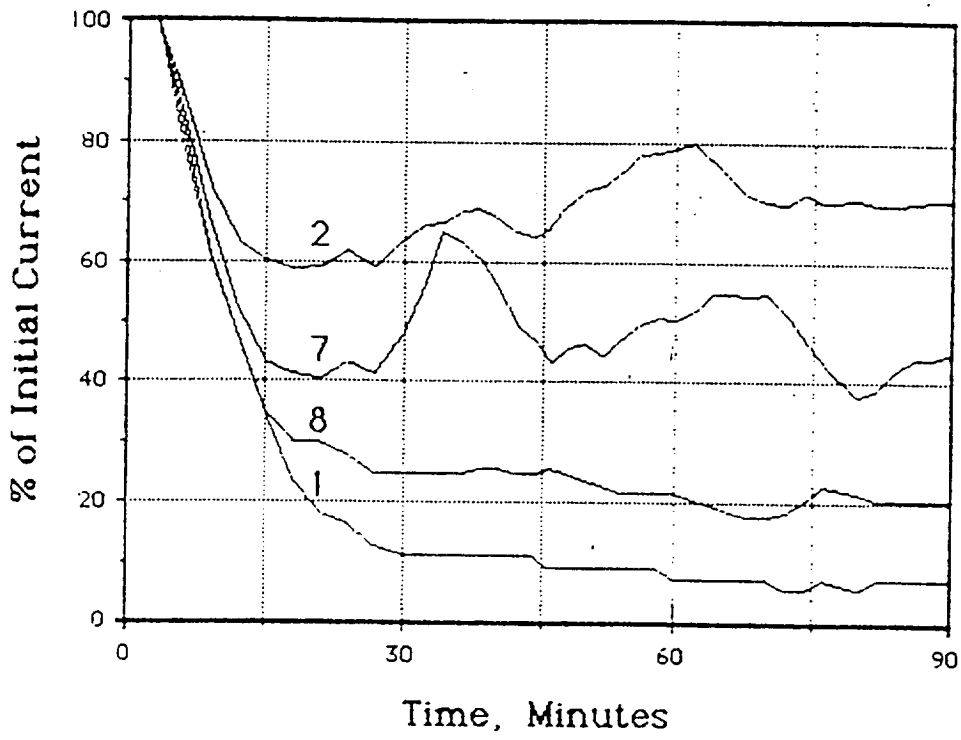

Rectangular Cells

Cell #2: 0.250 x 0.240"
Cell #7: 0.250 x 0.120"
Cell #8: 0.250 x 0.060"
Cell #1: 0.250 x 0.040"

Fig. 16 Plot of normalized current measurements versus time for cylindrical cells on the STS-26 mission.

Table 2a
Computer Simulation Data for Flight Experiments on STS-11

General Values

Column length	4.5 *cm*
Segmentation	100 segments
Current density	336.7 A/m^2*

pK_a and Mobility Values

Component	pK_{a1}	pK_{a2}	Mobility x 10^8 $[m^2/Vs]$	Conc. x 10^3 $[M]$
Arginine	9.04	12.48	2.71	8.0
Lysisl-Aspartate	4.1	7.7	2	10.0
p-ABA	2.41	4.85	3.28	6.0
Hemoglobin				0.0382
Albumin				0.0110

* This implies a constant voltage of 75.0 *V*.

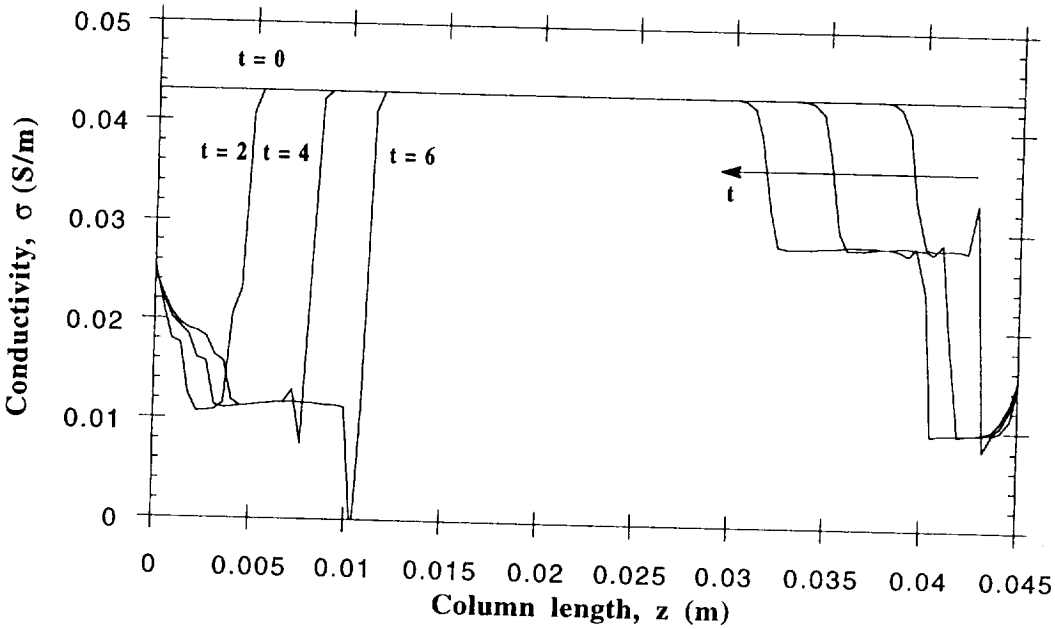

Fig. 17 Simulated evolution of the conductivity profile for the first six minutes in the IEF separation process for the system in Table 2a. The simulation failed past the sixth minute.

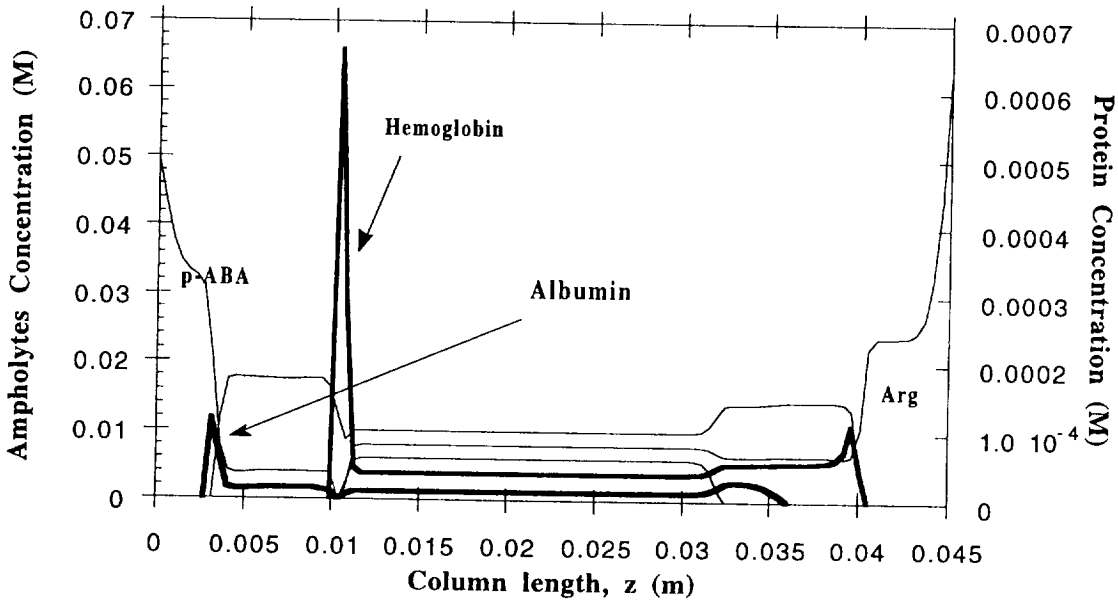

Fig. 18 Simulated concentration profile at 6 min into the simulation for the system in Table 2a. The simulation failed after the sixth minute.

necessary to re-run the simulation under conditions of reduced voltage. Furthermore, because small amounts of protein do not significantly alter the conductivity profile, the revised simulation was done for a three ampholyte solution (*sans* proteins). Input data for the revised simulation are given in Table 2b and the results are shown in Figs. 19-23. The evolution of the conductivity profile is depicted in Figs. 19 and 20. Here the rate of focusing of the components is slower than in the flight experiments because of the smaller current used. Notice that it is possible to distinguish the migrating zones at the different stages of the process. More importantly, recognize that at some time between 3 and 4 minutes into the simulation, a large conductivity gradient develops as the pure Lysil-Aspartate zone appears. These localized conductivity changes are accompanied by free charge accumulations, and it is at this stage that the conductivity gradients are postulated to favor the onset of EHD. The magnitude of the normalized conductivity gradient, $\nabla\sigma/\sigma$, is greater than 100 m^{-1}, as shown in Fig. 21. An estimate of the minimum conductivity gradient required to yield flow strengths of the order of those observed in the flight experiments is $\nabla\sigma/\sigma \approx 3\, m^{-1}$ (cf. Appendix 1). The simulations clearly show that, if the IEF solution were to remain quiescent, values for $\nabla\sigma/\sigma$ far in excess of 3 would develop (cf. Fig. 21). Thus, the IEF process proceeds in such a way that the requisite conditions are manifested for strong EHD floor. In Chapter 2, therefore, we take up the question of the onset of EHD convection in liquids that contain appreciable conductivity gradients. Note for completeness the steady-state pH, conductivity and concentration profiles are shown in Figs. 22 and 23.

Table 2b
Computer Simulation Data for Flight Experiments on STS-11

General Values

Column length	1.0 *cm*
Segmentation	200 segments
Current density	20 A/m^2*

pK_a and Mobility Values

Component	pK_{a1}	pK_{a2}	Mobility x 10^8 $[m^2/Vs]$	Conc. x 10^3 $[M]$
Arginine	9.04	12.48	2.71	8.0
Lysisl-Aspartate	4.1	7.7	2	10.0
p-ABA	2.41	4.85	3.28	6.0

* This implies a constant voltage of 11.53 *V*.

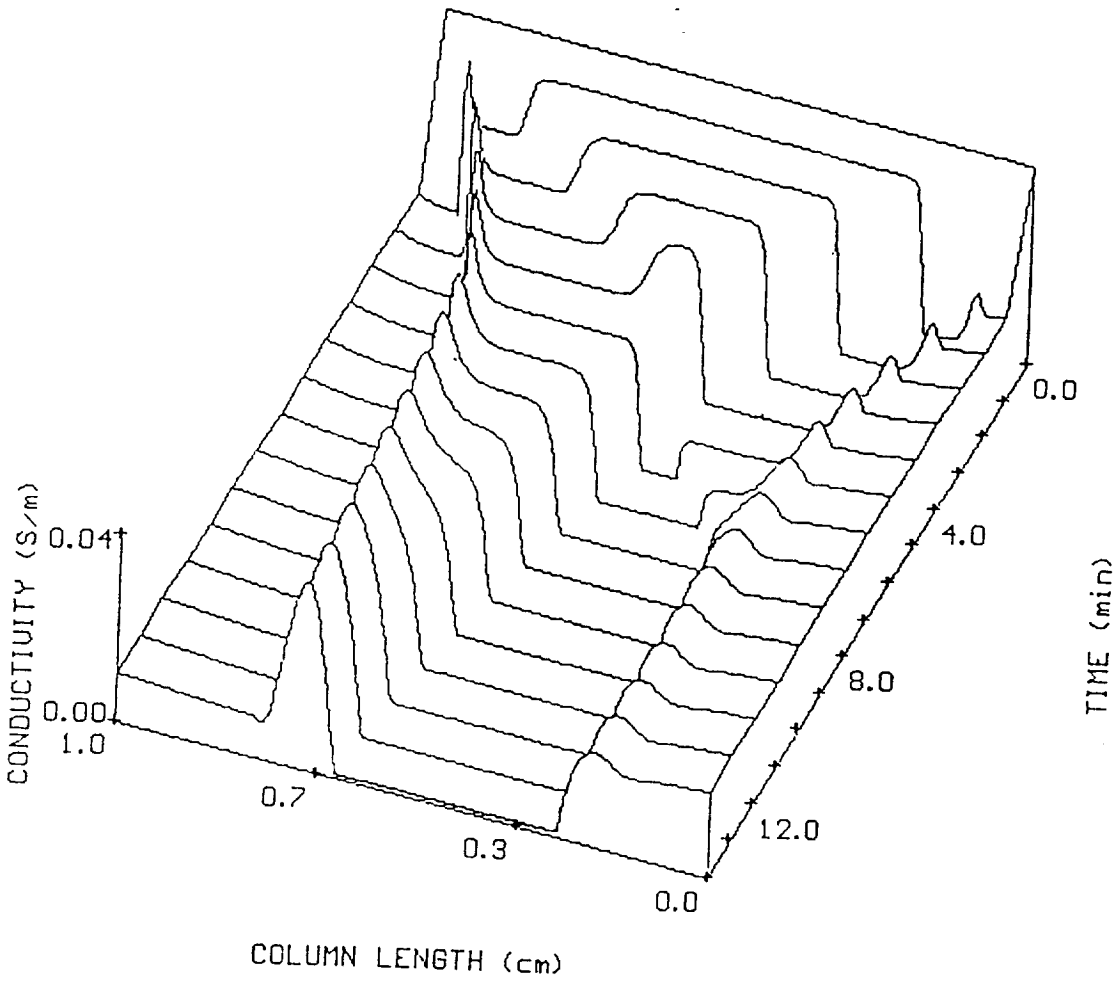

Fig. 19 The evolution of the conductivity profile during the IEF separation for the system in Table 2b.

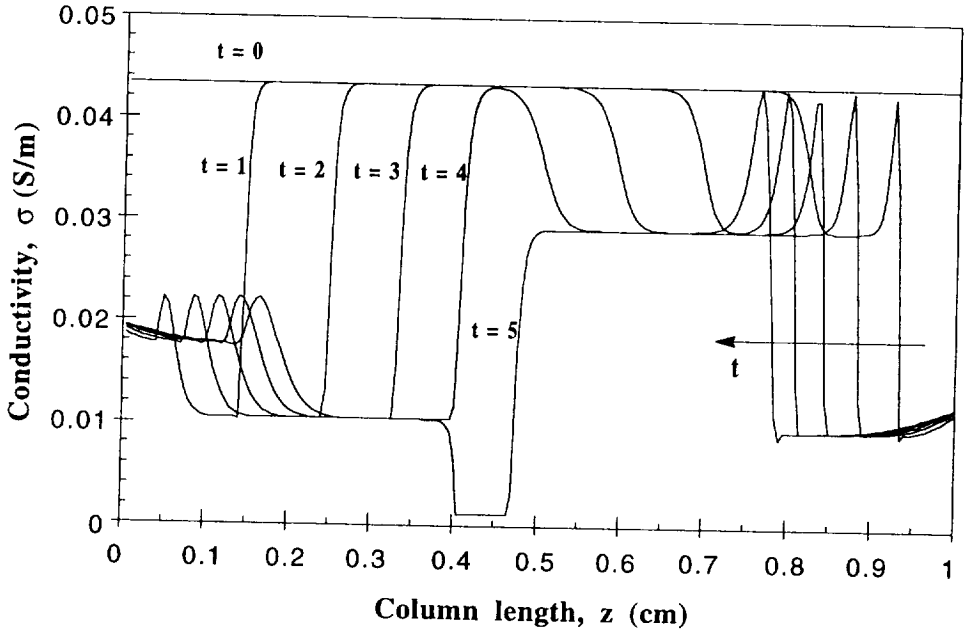

Fig. 20 Simulated conductivity profile for the first five minutes of the IEF separation process for the system in Table 2b.

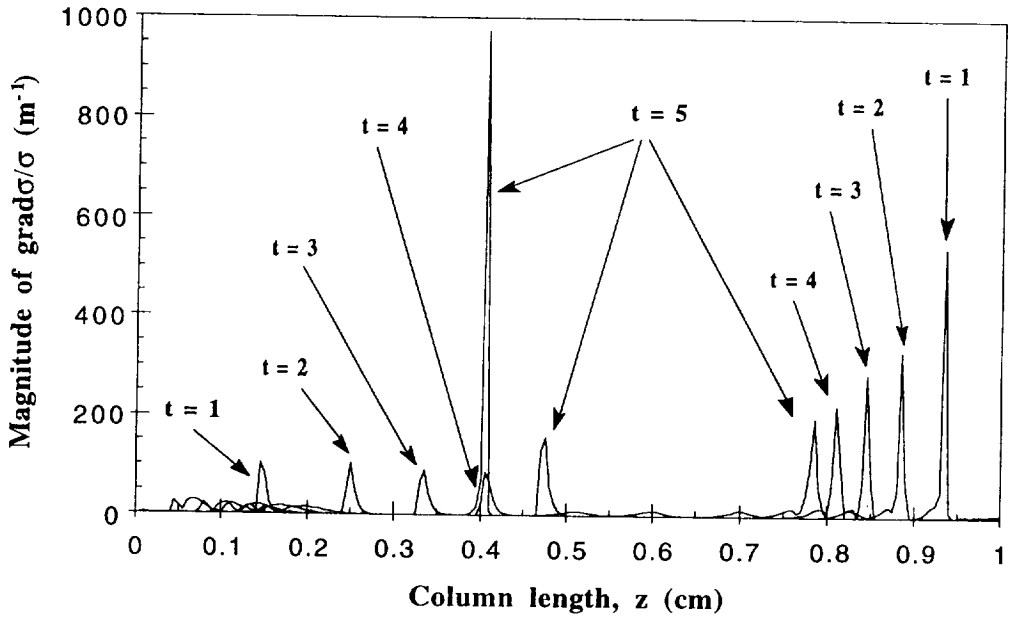

Fig. 21 Development of the conductivity gradient for the first five minutes of the simulated IEF separation for the system in Table 2b.

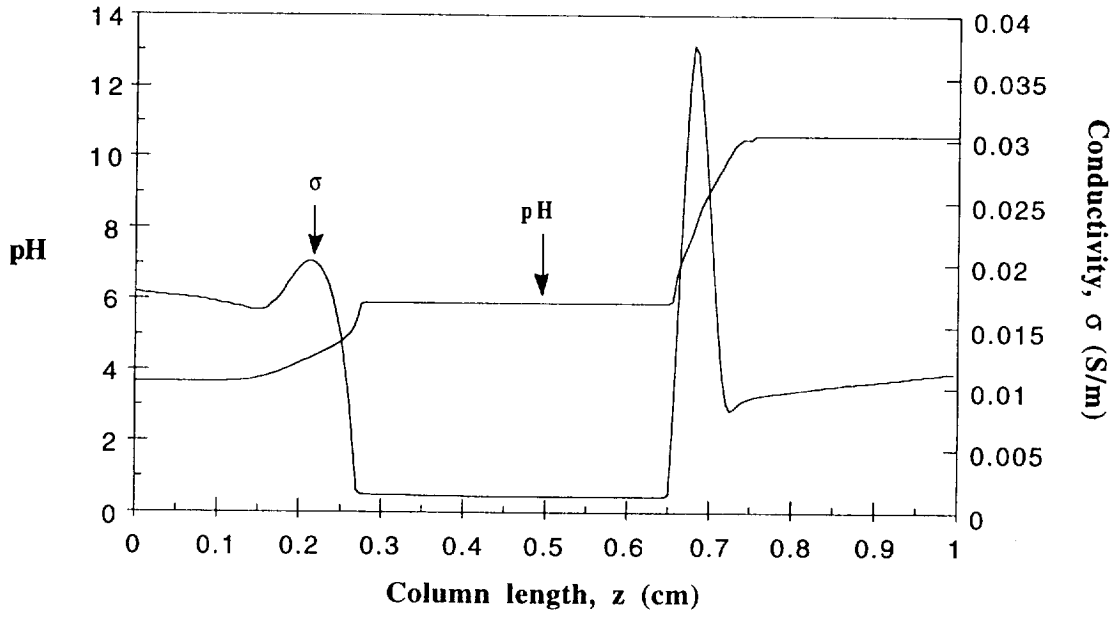

Fig. 22 Simulated steady state pH and conductivity profiles for the IEF separation for the system in Table 2b.

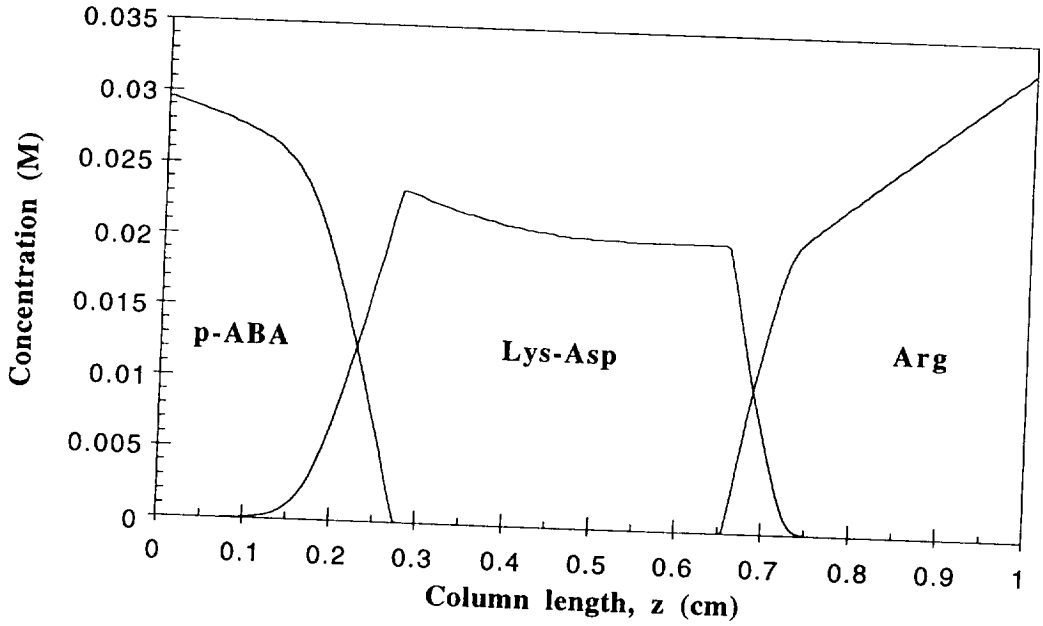

Fig. 23 Simulated steady state concentration profile for the system in Table 2b.

References

[1] Mosher, R.A., Saville, D.A. and Thormann, W., *The Dynamics of Electrophoresis*, VCH, 1992.

[2] Bier, M., Palusinski, R.A., Mosher, R.A. and Saville, D.A., *Science*, **219**, 1281-7 (1983).

[3] Thormann, W., Mosher, R.A. and Bier M., *Journal of Chromatography*, **351**, 17-29 (1986).

[4] Bier, M., *Hormone Purification by Isoelectric Focusing in Space*, Final Report, Contract NAS8-32950, 1990.

[5] Rhodes, P.H., Snyder, R.S. and Roberts, G.O., *J. Colloid Interface Sci.*, **129**, 78, 1989.

CHAPTER 2[†]: ELECTROHYDRODYNAMIC INSTABILITY IN A THIN FLUID LAYER WITH AN ELECTRICAL CONDUCTIVITY GRADIENT

Introduction

Electrohydrodynamic motion is known to occur in liquids where spatial gradients in the electrical properties are present. Classical examples of these flows are found in systems with step-changes in the electrical properties, such as those at the boundary between immiscible phases. Taylor and McEwan[1] analyzed the stability of a horizontal interface between two superposed liquids, and Michael and O'Neill[2] investigated the stability of a non-conducting layer sandwiched horizontally between two conducting fluids, in a vertical electric field. These studies show that, without the stabilizing effect of interfacial tension, the quiescent fluid arrangement is disrupted. Indeed, in a series of experiments on *miscible* laminar jets, Rhodes, *et al.*[3] demonstrated that, unimpeded by the restoring influence of interfacial tension, electrohydrodynamic stresses flatten cylindrical jets into ribbons. Still more examples of flows driven by interfacial electric stresses are reviewed by Melcher and Taylor[4].

Electrohydrodynamic motion has also been studied in systems where the spatial variations in the electrical properties are far less dramatic. Turnbull and Melcher[5] examined the stability of a perfectly insulating fluid layer in the presence of thermally-induced gradients in density, dielectric constant and viscosity. Variations in the dielectric constant give rise to dielectrophoretic body forces on the fluid and free charge accumulates in the bulk. It was shown that if a dc electric field is applied to the (quiescent) fluid layer,

[†] Extensive excerpts of this chapter have been submitted in June 1994 to *Physics of Fluids* for publication.

electrohydrodynamic instability sets in, provided that the thermal diffusion time is long compared with the charge relaxation time. Melcher and Firebaugh[6] studied fluid motion in semi-conducting liquids with thermally-induced conductivity gradients. They showed that, subject to a potential wave that travels orthogonal to the temperature gradient, the liquid flows anti-parallel to the conductivity gradient.

Here we consider the onset of electrohydrodynamic motion in a layer of liquid across which there is a continuous variation in the electrical conductivity; in contrast to Melcher and Firebaugh[6], we are concerned with conductivity variations associated with gradients in the concentration of charge-carrying solutes. A linear stability analysis is performed on the quiescent base state that exists when the conductivity varies linearly with position and there is an electric field applied across the layer of liquid. The conditions for marginal stability are determined, and the analysis shows that the relevant dimensionless groups are: Ra_e, an electric Rayleigh number; $\Delta\sigma/\sigma_0$, the relative conductivity increment; τ, the ratio of viscous to charge relaxation times; and α, the transverse wave number of the disturbance. Numerical calculations show that, for a given relative conductivity increment, the fluid layer becomes unstable when the electric Rayleigh number exceeds a certain value; the critical values for Ra_e and α depend solely on $\Delta\sigma/\sigma_0$ in the limit $\tau \to \infty$, which are the conditions for ohmic, aqueous systems.

The balance laws include the effects of diffusive processes associated with the conductivity profile and, so, the analysis differs from those of Hoburg and Melcher[7] and Hoburg[8] for the stability of fluid layers with colinear field and conductivity gradients. In their analyses, the conductivity gradients developed (quiescently) due to the diffusion of charge-carrying solutes, but these diffusive processes were then omitted from the equations governing the stability of the fluid layer. The rationale for such an approximation is that the time scale for diffusion of ionic solutes is typically quite long compared to the viscous

response time, i.e. $K_{\text{eff}}/\nu << 1$, where K_{eff} is an effective diffusivity for the conductivity [cf. Eq. (12)] and ν is the kinematic viscosity of the liquid.

In the present context, however, the electrical conductivity gradients are large. Thus, diffusive processes are important in spite of the fact that $K_{\text{eff}}/\nu << 1$. More specifically, diffusion of the ionic solutes tends to stabilizes the layer against the onset electrohydrodynamic motion. To see this, consider the fluid layer depicted in Fig. 1, where the electric field is directed parallel to the conductivity gradient. If a parcel of fluid within the layer is displaced upward, it moves to a region in which, locally, the conductivity is higher and the electric field is lower. It can be shown[9] that a low conductivity parcel surrounded by higher conductivity fluid will tend to migrate toward regions of lower field strengths. Such migration is driven by the gradient in the electric field and is referred to here as dielectrophoretic, though the effects are due to variations in the conductivity and *not* the dielectric constant of the medium. These dielectrophoretic effects favor continued upward movement of the fluid parcel. On the other hand, diffusive transport of charge-carrying solutes tends to eliminate the conductivity differences between the upwardly directed fluid parcel and its surroundings. If this diffusive transport is comparatively rapid, the upward motion of the parcel is arrested because the dielectrophoretic forces vanish with the conductivity difference. Note the fluid viscosity also tends to resist continued motion of the parcel. Depending on the relative strengths of these competing effects, which are embodied in Ra_e, the displaced fluid parcel may or may not continue upward—and this distinguishes unstable from stable base states. If K_{eff}/ν is set to zero, as was done by Hoburg and Melcher[7] and Hoburg,[8] the stabilizing influence of the diffusive processes is not captured and the fluid layer is made linearly unstable by the imposition of the external field. Such a result is analogous to what one would expect from the classical Rayleigh-Benard problem if, in writing the thermal energy balance for the perturbation variables, one were to consider the fluid to have zero thermal conductivity.

Interest in the present problem stems from electrically-driven convection observed in space-flight experiments on isoelectric focusing[10], a separation process used to isolate and purify biological materials[11]. Experimental measurements and numerical simulations[10-12] show that appreciable conductivity gradients develop during isoelectric focusing (IEF), and it has been postulated that these gradients precipitate the observed flows[3,10]. The conditions leading to the onset of motion in IEF are of concern because convection disrupts the separation process; the linear stability analysis is formulated here so as to describe conditions that give rise to such deleterious convection in initially quiescent fluid layers.

The presentation is organized as follows. First, the balance laws that govern the electrohydrodynamics of the fluid layer are presented, and then, after a brief scale analysis, they are placed in dimensionless form. Next, a linear stability analysis is performed; the quiescent base state is perturbed slightly, and the perturbations are examined. Finally the results of the analysis are discussed and concluding remarks are made.

Balance Laws

The electrical force acting on ionic solutes is transferred to the solvent through collisions at the molecular level. The free charges individually transfer their momentum to the solvent, so the Navier-Stokes equations, which govern the fluid motion, must be modified to read

$$\rho\left(\frac{\partial \mathbf{v}}{\partial t}+\mathbf{v}\cdot\nabla\mathbf{v}\right)=-\nabla p+\mu\nabla^2\mathbf{v}+\mathbf{f}_e\,, \qquad (1)$$

where $\mathbf{f}_e$ is the electrical force on the solvent per unit volume. Provided that the electric displacement $\mathbf{D}$ and the electric field $\mathbf{E}$ are co-linear, $\mathbf{f}_e$ can be expressed in terms of the Maxwell stress tensor[13,14], viz.

$$\mathbf{f}_e = \nabla \cdot \mathbf{T}\,, \tag{2}$$

where for an incompressible linear dielectric,

$$\mathbf{T} = \mathbf{ED} - \frac{1}{2\varepsilon}(\mathbf{D}\cdot\mathbf{D})\,\mathbf{I}\,. \tag{3}$$

Since $\mathbf{D} = \varepsilon\mathbf{E}$ and $\rho_f = \nabla \cdot \mathbf{D}$,

$$\mathbf{f}_e = \rho_f \mathbf{E} - \frac{1}{2}(\mathbf{E}\cdot\mathbf{E})\nabla\varepsilon\,. \tag{4}$$

The first term on the right hand side of Eq. (4) is the (coulombic) electrical body force caused by the action of the electric field on ρ_f, the free charge density in solution. The second term accounts for electric forces due to gradients of the dielectric constant ε. When Eq. (4) is combined with Eq. (1), the momentum balance becomes

$$\rho\frac{D\mathbf{v}}{Dt} = -\nabla p + \rho_f\mathbf{E} - \frac{1}{2}(\mathbf{E}\cdot\mathbf{E})\nabla\varepsilon + \mu\nabla^2\mathbf{v}\,, \tag{5}$$

with

$$\nabla\cdot\mathbf{v} = 0\,. \tag{6}$$

Analysis of Eq. (5) is often difficult because, according to Maxwell's equations, the electric field is coupled to the free charge density ρ_f. Moreover, the free charge density is influenced by convection, so one may not generally specify ρ_f and $\mathbf{E}$ independently of $\mathbf{v}$. As long as the electrical current density $\mathbf{J}_f$ is modest, $\mathbf{E}$ is quasi-static, so that

$$\nabla\times\mathbf{E} = \mathbf{0} \tag{7}$$

and

$$\nabla \cdot (\varepsilon \mathbf{E}) = \rho_f \, . \tag{8}$$

This latter relation is Gauss' law. Conservation of charge requires

$$\frac{\partial \rho_f}{\partial t} + \nabla \cdot \mathbf{J}_f = 0 \, . \tag{9}$$

For ohmic conductors the current density is given by[13,14]

$$\mathbf{J}_f = \sigma \mathbf{E} + \mathbf{v} \, \rho_f \, , \tag{10}$$

where σ is the electrical conductivity and the second term on the right hand side represents convection of free charge. Combining Eqs. (9) and (10) yields

$$\frac{D\rho_f}{Dt} = \nabla\sigma \cdot \mathbf{E} + \sigma \nabla \cdot \mathbf{E} \, , \tag{11}$$

since $\nabla \cdot \mathbf{v} = 0$.

Because the solution is an ionic conductor, the conductivity depends on the local ion concentration. As a result, the conductivity may vary with position and time. Melcher[13,14] has shown that the evolution of the conductivity profile is satisfactorily described by

$$\frac{D\sigma}{Dt} = K_{eff} \nabla^2 \sigma \, , \tag{12}$$

where K_{eff} represents an effective diffusivity that arises due to Brownian motion of the ions. Though Eq. (12) appears to be a balance on a physical property it should be recognized that, in ionic conductors the conductivity varies locally with the concentration of charge-carrying solutes. Equation (12) holds[14] provided that the local charge accumulations relax rapidly compared to the time necessary for momentum transfer (viscous relaxation time) and the time required for ion electro-migration, viz.

$$\frac{\varepsilon}{\sigma_0} << \frac{d}{\omega E_0} << \frac{d^2}{\nu} \text{ and } \frac{d^2}{\omega k_B T},$$

where ω is a characteristic mobility of the charge-carrying solutes and $k_B T$ is the Boltzmann temperature.

Scale Analysis

As an IEF experiment proceeds, concentration, pH and conductivity gradients develop along the axis of the imposed electric field. Simulations show[11,12,15] that, if the process proceeds without convection, the local conductivity can vary by more than an order of magnitude over a length of $1mm$. The diameter of a cylindrical IEF separation chamber is roughly $1cm$ and the chamber is several cm long, so the axial distance over which the conductivity gradients occur is thin compared to radial and axial dimensions of the chamber, and the region of variation is distant from either electrode[11,12,15].

For the situation depicted in Fig. 1, the conductivity profile $\overline{\sigma}^*(z^*)$ varies linearly across the domain $0 \le z^* \le d$[16]. It can be readily seen that such a conductivity profile satisfies the conditions for a steady and quiescent base state. If $\overline{\sigma}^*$ is expressed as

$$\overline{\sigma}^*(z^*) = \sigma_0 + \frac{\sigma_d - \sigma_0}{d} z^* = \sigma_0 + \frac{\Delta\sigma}{d} z^*, \qquad (13)$$

it follows that

$$\frac{\partial^2 \overline{\sigma}^*(z^*)}{\partial z^{*2}} \equiv 0 \,, \tag{14}$$

and according to Eq. (12) the conductivity profile is steady.

The base state solution associated with Eq. (13) is:

$$\overline{\mathbf{E}}^*(z^*) = \frac{1}{1+\left(\frac{\Delta\sigma}{\sigma_0}\right)\frac{z^*}{d}} E_0 \, \hat{\mathbf{i}}_z \,; \tag{15}$$

$$\overline{p}^*(z^*) = \frac{1}{2}\varepsilon \frac{1}{\left(1+\frac{\Delta\sigma}{\sigma_0}\frac{z^*}{d}\right)^2} E_0^2 + p_0^* \,; \tag{16}$$

$$\overline{\rho}_f^*(z^*) = -\varepsilon \frac{\Delta\sigma/\sigma_0}{\left(1+\frac{\Delta\sigma}{\sigma_0}\frac{z^*}{d}\right)^2} \frac{E_0}{d} \,; \tag{17}$$

$$\overline{\mathbf{v}}^*(z^*) \equiv 0 \,. \tag{18}$$

Here p_0^* is the ambient pressure, E_0 is the electric field strength at the lower boundary in the base state (from Eq. (15)) and $E_0\sigma_0 = J_0$, i.e., there is a constant current density J_0 across the fluid layer in the base state.

The base-state solution suggests the following reference scales, which are used to place the balance laws in dimensionless form: free charge density, $\varepsilon E_0 \Delta\sigma / d\sigma_0$; electric

field, E_0; and length, d. Hereafter, σ denotes the dimensionless conductivity, i.e. $\sigma \equiv (\sigma^* - \sigma_0)/\Delta\sigma$.

The *dimensionless* momentum balance reads

$$\frac{D\mathbf{v}}{Dt} = -\nabla p + \frac{1}{\sqrt{Gr_e}}\nabla^2\mathbf{v} + \rho_f \mathbf{E}\,, \tag{19}$$

where the variables are now in scaled form. A balance of the inertial and electrical effects requires that the velocity scale be $\sqrt{\varepsilon E_0^2 \Delta\sigma/\rho\sigma_0}$, and the appropriate stress scale is $\varepsilon E_0^2 \Delta\sigma/\sigma_0$; the time scale is $\sqrt{d^2\rho\sigma_0/\varepsilon E_0^2\Delta\sigma}$. The dimensionless group that appears in Eq. (19) is defined by

$$Gr_e \equiv \frac{d^2}{\nu^2}\frac{\varepsilon E_0^2}{\rho}\frac{\Delta\sigma}{\sigma_0}\,, \tag{20}$$

and can be thought of as an electric Grashof number, since Gr_e is a measure of the relative strength of electrical body forces and viscous effects. The inertial scaling chosen here is appropriate when Gr_e is $O(1)$ or more.

The governing equation for the evolution of the electrical conductivity becomes

$$\frac{D\sigma}{Dt} = \frac{1}{Sc_e\sqrt{Gr_e}}\nabla^2\sigma\,, \tag{21}$$

if an electric Schmidt number is defined as

$$Sc_e \equiv \frac{\nu}{K_{eff}}. \tag{22}$$

Here Sc_e is roughly $10^3 - 10^6$, since K_{eff} ranges from $10^{-9} - 10^{-12} m^2/s$.

The conservation of charge relation transforms to

$$\frac{D\rho_f}{Dt} = -\frac{1}{\sqrt{Gr_e}} \frac{d^2\sigma_0}{\nu\varepsilon} \left\{ \left[1 + \frac{\Delta\sigma}{\sigma_0}\sigma \right] \rho_f + \mathbf{E} \cdot \nabla\sigma \right\}, \tag{23}$$

where $\tau \equiv d^2\sigma_0/\nu\varepsilon$ represents the viscous relaxation time of the liquid normalized to ε/σ_0, the charge relaxation time in a liquid of conductivity σ_0 and dielectric constant ε. For electrolytic buffer solutions $\sigma_0 \approx 10^{-2}$ S/m and $\varepsilon \approx 10^{-9}\, C/(m \times V)$, so $d^2\sigma_0/\nu\varepsilon$ is $O(10^8)$ when $d \approx 10^{-3} m$ and $\nu \approx 10^{-6} m^2/s$.

Gauss' law in dimensionless form is

$$\nabla \cdot \mathbf{E} = \frac{\Delta\sigma}{\sigma_0}\rho_f \,. \tag{24}$$

Because the electric field is irrotational, the electric potential can be introduced, viz.

$$\mathbf{E} = -\nabla\phi \,, \tag{25}$$

and then Eq. (23) becomes

$$\frac{D}{Dt}\left(\nabla^2\phi\right) = -\frac{\tau}{\sqrt{Gr_e}} \left\{ \left[1 + \frac{\Delta\sigma}{\sigma_0}\sigma \right] \nabla^2\phi + \frac{\Delta\sigma}{\sigma_0} \nabla\phi \cdot \nabla\sigma \right\}. \tag{26}$$

Similarly, substituting Eqs. (24) and (25) into Eq. (19) yields

$$\frac{D\mathbf{v}}{Dt} = -\nabla p + \frac{1}{\sqrt{Gr_e}}\nabla^2\mathbf{v} + \frac{\sigma_0}{\Delta\sigma}\left(\nabla^2\phi\right)\nabla\phi \,. \tag{27}$$

Equations (26) and (27), along with Eqs. (6) and (21), are the balance laws used to describe the dynamic behavior of the system whose base state is depicted in Fig. 1. In the next section, a linear stability analysis is performed on this base state. Small perturbations are introduced to the system and their evolution is analyzed to determine if the disturbances grow or decay with time.

Linear Stability Analysis

The base-state solution in dimensionless form is:

$$\overline{\sigma}(z) = z \,; \tag{28}$$

$$\overline{E}(z) = \frac{1}{1+\dfrac{\Delta\sigma}{\sigma_0}z} \,; \tag{29}$$

$$\overline{p}(z) = \frac{1}{2}\frac{\sigma_0/\Delta\sigma}{\left(1+\dfrac{\Delta\sigma}{\sigma_0}z\right)^2} + \overline{p}_0 \,; \tag{30}$$

$$\overline{\rho}_f(z) = -\frac{1}{\left(1+\dfrac{\Delta\sigma}{\sigma_0}z\right)^2} \,; \tag{31}$$

$$\overline{v}(z) = 0 \,. \tag{32}$$

Note that overbars indicate the base-state variables.

To carry out a linear stability analysis of the base state, the following perturbation variables are introduced[17-19]:

$$\mathbf{v}(\mathbf{x},t) = \mathbf{v}'(\mathbf{x},t) = u'(\mathbf{x},t)\,\mathbf{i}_x + \mathrm{v}'(\mathbf{x},t)\,\mathbf{i}_y + w'(\mathbf{x},t)\,\mathbf{i}_z\ ; \tag{33}$$

$$\sigma(\mathbf{x},t) = \overline{\sigma}(z) + \sigma'(\mathbf{x},t)\ ; \tag{34}$$

$$\phi(\mathbf{x},t) = \overline{\phi}(z) + \phi'(\mathbf{x},t)\ ; \tag{35}$$

$$p(\mathbf{x},t) = \overline{p}(z) + p'(\mathbf{x},t)\ ; \tag{36}$$

where the prime denotes the perturbation variables, and

$$\overline{\phi}(z) = \phi_0 - \int_0^z \overline{E}(\xi)d\xi = \phi_0 - \frac{\sigma_0}{\Delta\sigma}\ln\left(1 + \frac{\Delta\sigma}{\sigma_0}z\right). \tag{37}$$

Formal substitution of Eqs. (33)-(37) into the balance laws yields

$$\frac{\partial \mathbf{v}'}{\partial t} = -\nabla p' + \frac{1}{\sqrt{Gr_e}}\nabla^2\mathbf{v}' + \frac{\sigma_0}{\Delta\sigma}\left\{\frac{d\overline{\phi}}{dz}\nabla^2\phi'\,\mathbf{i}_z + \frac{d^2\overline{\phi}}{dz^2}\nabla\phi'\right\}, \tag{38}$$

$$\frac{\partial \sigma'}{\partial t} + w'\frac{d\overline{\sigma}}{dz} = \frac{1}{Sc_e\sqrt{Gr_e}}\nabla^2\sigma', \tag{39}$$

$$\frac{\partial}{\partial t}\left(\nabla^2\phi'\right) + \frac{d^3\overline{\phi}}{dz^3}w' = -\frac{\tau}{\sqrt{Gr_e}}\left\{\left[1 + \frac{\Delta\sigma}{\sigma_0}\overline{\sigma}\right]\nabla^2\phi' +\right.$$

$$\frac{\Delta\sigma}{\sigma_0}\left[\frac{d^2\bar{\phi}}{dz^2}\sigma' + \frac{d\bar{\sigma}}{dz}\frac{\partial\phi'}{\partial z} + \frac{d\bar{\phi}}{dz}\frac{\partial\sigma'}{\partial z}\right]\Bigg\}, \tag{40}$$

and

$$\nabla\cdot\mathbf{v}' = 0\,, \tag{41}$$

upon linearization. The pressure and the x and y components of the velocity are eliminated from the problem by taking the curl of the momentum balance and making use of continuity. The resulting expression is

$$\left(\frac{\partial}{\partial t} - \frac{1}{\sqrt{Gr_e}}\nabla^2\right)\nabla^2 w' = \frac{\sigma_0}{\Delta\sigma}\frac{d\bar{\phi}}{dz}\nabla^2\left(\nabla_1^2\phi'\right) - \frac{\sigma_0}{\Delta\sigma}\frac{d^3\bar{\phi}}{dz^3}\nabla_1^2\phi'\,, \tag{42}$$

with

$$\nabla_1^2 \equiv \frac{\partial^2}{\partial x^2} + \frac{\partial^2}{\partial y^2}.$$

Equations (39), (40) and (42) are a coupled set of partial differential equations and the unknowns to be determined are: $w'(\mathbf{x},t)$, the perturbation in the z-component of the velocity; $\phi'(\mathbf{x},t)$, the perturbation in the electric potential; and $\sigma'(\mathbf{x},t)$, the perturbation in the conductivity.

Equations (39), (40) and (42) are linear and symmetric in x and y, and, so, are amenable to a normal modes analysis. Accordingly the solutions for the perturbation variables are assumed to have the form

$$\left.\begin{matrix} w'(\mathbf{x},t) \\ \phi'(\mathbf{x},t) \\ \sigma'(\mathbf{x},t) \end{matrix}\right\} = \left\{\begin{matrix} \hat{w}'(z) \\ \hat{\phi}'(z) \\ \hat{\sigma}'(z) \end{matrix}\right\} f(x,y)e^{st}\,. \tag{43}$$

There are solutions of similar form for $p'(\mathbf{x},t)$, $u'(\mathbf{x},t)$, $v'(\mathbf{x},t)$ and $E'(\mathbf{x},t)$. Formal substitution of Eq. (43) into Eqs. (39), (40) and (42) yields

$$\left(\frac{\partial}{\partial t}-\frac{1}{\sqrt{Gr_e}}\nabla^2\right)\nabla^2\left(\hat{w}'fe^{st}\right)=\frac{\sigma_0}{\Delta\sigma}\frac{d\overline{\phi}}{dz}\nabla^2\left(\nabla_1^2\left(\hat{\phi}'fe^{st}\right)\right)-\frac{\sigma_0}{\Delta\sigma}\frac{d^3\overline{\phi}}{dz^3}\nabla_1^2\left(\hat{\phi}'fe^{st}\right), \tag{44}$$

$$\left(\frac{\partial}{\partial t}-\frac{1}{Sc_e\sqrt{Gr_e}}\nabla^2\right)\left(\hat{\sigma}'fe^{st}\right)=-\frac{d\overline{\sigma}}{dz}\left(\hat{w}'fe^{st}\right), \tag{45}$$

$$\left\{\frac{\partial}{\partial t}+\frac{\tau}{\sqrt{Gr_e}}\left[1+\frac{\Delta\sigma}{\sigma_0}\overline{\sigma}\right]\right\}\nabla^2\left(\hat{\phi}'fe^{st}\right)+\frac{d^3\overline{\phi}}{dz^3}\left(\hat{w}'fe^{st}\right)=$$
$$-\frac{\tau}{\sqrt{Gr_e}}\frac{\Delta\sigma}{\sigma_0}\left\{\frac{d^2\overline{\phi}}{dz^2}\left(\hat{\sigma}'fe^{st}\right)+\frac{d\overline{\sigma}}{dz}\frac{\partial\left(\hat{\phi}'fe^{st}\right)}{\partial z}+\frac{d\overline{\phi}}{dz}\frac{\partial\left(\hat{\sigma}'fe^{st}\right)}{\partial z}\right\}. \tag{46}$$

Based on Eq. (45), a form of the disturbances in the x and y directions can be determined[19], viz.

$$f(x,y)=e^{i(\alpha_x x+\alpha_y y)}$$

with $$\alpha^2=\alpha_x^2+\alpha_y^2\,.$$

Equations (44)-(46) then become,

$$\left(s-\frac{1}{\sqrt{Gr_e}}\left(D^2-\alpha^2\right)\right)\left(D^2-\alpha^2\right)\hat{w}'=-\alpha^2\frac{\sigma_0}{\Delta\sigma}\frac{d\overline{\phi}}{dz}\left(D^2-\alpha^2\right)\hat{\phi}'+\alpha^2\frac{\sigma_0}{\Delta\sigma}\frac{d^3\overline{\phi}}{dz^3}\hat{\phi}', \tag{47}$$

$$\left(s-\frac{1}{Sc_e\sqrt{Gr_e}}\left(D^2-\alpha^2\right)\right)\hat{\sigma}'=-\frac{d\overline{\sigma}}{dz}\hat{w}', \tag{48}$$

$$\left\{s+\frac{\tau}{\sqrt{Gr_e}}\left[1+\frac{\Delta\sigma}{\sigma_0}\overline{\sigma}\right]\right\}\left(D^2-\alpha^2\right)\hat{\phi}'+\frac{d^3\overline{\phi}}{dz^3}\hat{w}'=$$
$$-\frac{\tau}{\sqrt{Gr_e}}\frac{\Delta\sigma}{\sigma_0}\left\{\frac{d^2\overline{\phi}}{dz^2}\hat{\sigma}'+\frac{d\overline{\sigma}}{dz}D\hat{\phi}'+\frac{d\overline{\phi}}{dz}D\hat{\sigma}'\right\}. \tag{49}$$

From the base state solutions,

$$\frac{d\overline{\sigma}}{dz}=1\ ;$$

$$\frac{d\overline{\phi}}{dz}=-\frac{1}{1+\frac{\Delta\sigma}{\sigma_0}z}\ ;\quad \frac{d^2\overline{\phi}}{dz^2}=\frac{\Delta\sigma}{\sigma_0}\frac{1}{\left(1+\frac{\Delta\sigma}{\sigma_0}z\right)^2}\ ;\quad \frac{d^3\overline{\phi}}{dz^3}=-2\left(\frac{\Delta\sigma}{\sigma_0}\right)^2\frac{1}{\left(1+\frac{\Delta\sigma}{\sigma_0}z\right)^3}.$$

Substitution of the above relations into Eqs. (47)-(49) yields

$$\left(s-\frac{1}{\sqrt{Gr_e}}\left(D^2-\alpha^2\right)\right)\left(D^2-\alpha^2\right)\hat{w}'=\alpha^2\frac{\sigma_0}{\Delta\sigma}\frac{1}{\left(1+\frac{\Delta\sigma}{\sigma_0}z\right)}\left(D^2-\alpha^2\right)\hat{\phi}'$$
$$-2\alpha^2\frac{\Delta\sigma}{\sigma_0}\frac{1}{\left(1+\frac{\Delta\sigma}{\sigma_0}z\right)^3}\hat{\phi}', \tag{50}$$

$$\left(s-\frac{1}{Sc_e\sqrt{Gr_e}}\left(D^2-\alpha^2\right)\right)\hat{\sigma}'=-\hat{w}', \tag{51}$$

$$\left\{s+\frac{\tau}{\sqrt{Gr_e}}\left[1+\frac{\Delta\sigma}{\sigma_0}z\right]\right\}\left(D^2-\alpha^2\right)\hat{\phi}'-2\left(\frac{\Delta\sigma}{\sigma_0}\right)^2\frac{1}{\left(1+\frac{\Delta\sigma}{\sigma_0}z\right)^3}\hat{w}'=$$

$$-\frac{\tau}{\sqrt{Gr_e}}\frac{\Delta\sigma}{\sigma_0}\left\{\frac{\Delta\sigma}{\sigma_0}\frac{1}{\left(1+\frac{\Delta\sigma}{\sigma_0}z\right)^2}\hat{\sigma}'+D\hat{\phi}'-\frac{1}{\left(1+\frac{\Delta\sigma}{\sigma_0}z\right)}D\hat{\sigma}'\right\}. \qquad (52)$$

The above set of equations, Eqs. (50)-(52), is a coupled system of ordinary differential equations in z; two equations of the set have coefficients that vary with z. The set of ODEs is solved with the following choice of boundary conditions: the electric field, velocity and conductivity are fixed at their base-state values on the upper and lower boundaries, i.e. $d\hat{\phi}'/dz=\hat{w}'=\hat{\sigma}'=0$ at $z=0$ and 1, and the boundaries are either stress-free, i.e. $d^2\hat{w}'/dz^2=0$, or rigid, i.e. $d\hat{w}'/dz=0$. These boundary conditions are consistent with the constant current imposed in the base state: $\bar{J}^*(z^*)=J_0=E_0\sigma_0$ for $0\le z^*\le d$. Note that $\mathbf{J}'=0$ at $z=0$ and 1. The eigensolutions to Eqs. (50)-(52) may be determined numerically for each wave number α, but some insight into the stability problem may be gained by manipulating the equations further.

First let $\tau\to\infty$, which is a reasonable approximation because the relaxation time of the charge ε/σ_0 is of $O(10^8)$ times faster than the characteristic relaxation time of the fluid. Then, for neutral stability ($s\equiv 0$), Eqs. (50)-(52) read

$$-\frac{1}{\sqrt{Gr_e}}\left(D^2-\alpha^2\right)^2\hat{w}'=\frac{\alpha^2}{\frac{\Delta\sigma}{\sigma_0}\left(1+\frac{\Delta\sigma}{\sigma_0}z\right)}\left(D^2-\alpha^2\right)\hat{\phi}'-2\alpha^2\frac{\Delta\sigma}{\sigma_0}\frac{1}{\left(1+\frac{\Delta\sigma}{\sigma_0}z\right)^3}\hat{\phi}', \qquad (53)$$

$$-\frac{1}{Sc_eGr_e}\left(D^2-\alpha^2\right)\hat{\sigma}'=-\frac{1}{\sqrt{Gr_e}}\hat{w}', \qquad (54)$$

$$\left[1+\frac{\Delta\sigma}{\sigma_0}z\right]\left(D^2-\alpha^2\right)\hat{\phi}' = -\frac{\Delta\sigma}{\sigma_0}\left\{\frac{\Delta\sigma}{\sigma_0}\frac{1}{\left(1+\frac{\Delta\sigma}{\sigma_0}z\right)^2}\hat{\sigma}' + D\hat{\phi}' - \frac{1}{\left(1+\frac{\Delta\sigma}{\sigma_0}z\right)}D\hat{\sigma}'\right\}. \quad (55)$$

Substituting Eq. (54) into (53) yields

$$-\frac{1}{Sc_eGr_e}\left(D^2-\alpha^2\right)^3\hat{\sigma}' = \frac{\alpha^2}{\frac{\Delta\sigma}{\sigma_0}\left(1+\frac{\Delta\sigma}{\sigma_0}z\right)}\left(D^2-\alpha^2\right)\hat{\phi}' - 2\alpha^2\frac{\Delta\sigma}{\sigma_0}\frac{1}{\left(1+\frac{\Delta\sigma}{\sigma_0}z\right)^3}\hat{\phi}'. \quad (56)$$

Notice Eqs. (55) and (56) can be solved for $\hat{\sigma}'$ and $\hat{\phi}'$ without reference to $\hat{w}'$; the only parameters that appear in these two equations are $\Delta\sigma/\sigma_0$, Sc_eGr_e and α. Moreover Eq. (54) shows that in order for $\hat{w}' \neq 0$, it must be that $\hat{\sigma}' \neq 0$. Thus the conditions for marginal stability (with α finite and $\tau \to \infty$) depend only on three parameters, viz. $\Delta\sigma/\sigma_0$, Sc_eGr_e and α. This is confirmed by the numerical results shown in section VI.

The product Sc_eGr_e can be thought of as an electric Rayleigh number, $Ra_e \equiv Sc_eGr_e \equiv d^2\varepsilon E_0^2\Delta\sigma/\mu K_{\text{eff}}\sigma_0$. If the characteristic velocity $\sqrt{\varepsilon E_0^2\Delta\sigma/\sigma_0\rho}$ is denoted by u_c, then one interpretation of Ra_e is as follows: $\left(\varepsilon E_0^2\Delta\sigma/\sigma_0\right)/\left(\mu u_c/d\right)$ is the ratio of electrical to viscous stresses; and u_cd/K_{eff} is a Peclet number that represents the relative strength of convective and diffusive transport of the conductivity fluctuations. So

$$Ra_e = \frac{\varepsilon E_0^2\,\Delta\sigma/\sigma_0}{\mu u_c/d}\frac{u_cd}{K_{\text{eff}}}$$

is a parameter that weighs the destabilizing effects of the electrical stresses against the stabilizing influence of viscosity, as well as the mechanisms that govern the evolution and transport of conductivity perturbations: convection (destabilizing) and diffusion (stabilizing).

Numerical Approach to the Neutral Stability Analysis

To generate the neutral stability curves for Eqs. (50)-(52), the conditions for which there are eigensolutions to Eqs. (50)-(52) (with $s \equiv 0$) were found by the following numerical technique. Equations (50)-(52) were first re-cast as a set of eight first order ODEs in z. The general numerical solution to the system of eight ODEs was constructed for specified values of Sc_e, Gr_e, $\Delta\sigma/\sigma_0$ and α. This was done by solving the system of equations for each of eight linearly independent sets of initial conditions (prescribed at the lower boundary, $z = 0$) and the integration was carried out using the IMSL Library routine DIVPAG. If $\mathbf{y}_i$ denotes the i^{th} linearly independent solution to the system of eight ODEs, the general (numerical) solution to the system can be written as

$$\mathbf{y} = \sum_{i=1}^{8} c_i \mathbf{y}_i ,$$

where the c_i are arbitrary constants. The general solution $\mathbf{y}$ must satisfy, for example, the following set of conditions at the (stress-free) boundaries:

$$\left.\begin{aligned}
&\left.\frac{d\hat{\phi}'}{dz}\right|_{z=0} = \left.\frac{d\hat{\phi}'}{dz}\right|_{z=1} = 0 \\
&\hat{w}'(z=0) = \hat{w}'(z=1) = 0 \\
&\hat{\sigma}'(z=0) = \hat{\sigma}'(z=1) = 0 \\
&\left.\frac{d^2\hat{w}'}{dz^2}\right|_{z=0} = \left.\frac{d^2\hat{w}'}{dz^2}\right|_{z=1} = 0 .
\end{aligned}\right\} \qquad (57)$$

The task of satisfying Eq. (57) consists, at least conceptually, of choosing the appropriate values for the c_i $(i = 1,2,...,8)$. To determine these values, one must solve an 8×8 system of linear algebraic equations, which can be expressed in the form

$$\mathbf{Ac} = \mathbf{0}, \quad \mathbf{c} = \begin{bmatrix} c_1 \\ c_2 \\ \vdots \\ c_8 \end{bmatrix}.$$

The elements of the matrix $\mathbf{A}$ depend on $\mathbf{y}_i(0)$ and $\mathbf{y}_i(1)$, the linearly independent solutions evaluated at $z = 0$ and 1, respectively, as well as Sc_e, Gr_e, etc. Now the ODEs and the initial conditions are a set of homogeneous equations. As such, solutions for $\hat{\sigma}'(z)$, $\hat{\phi}'(z)$ and $\hat{w}'(z)$ that satisfy Eqs. (50)-(52) and Eq. (57) are generally trivial, i.e.

$$\mathbf{Ac} = \mathbf{0} \Rightarrow \mathbf{c} = \mathbf{0} \Rightarrow \mathbf{y} = \mathbf{0}.$$

However for certain combinations of Sc_e, Gr_e, etc., nontrivial solutions do exist; these are commonly known as the eigensolutions to the problem and they obtain when $\det \mathbf{A} = 0$. A

search of the parameter space was implemented to establish the conditions for which $\det \mathbf{A} = 0$; this was done by varying Gr_e, while holding all other parameters fixed. The conditions thus delineated are used to plot the neutral or marginal stability curves presented in the following section.

Results and Discussion

Results for the neutral stability curves are shown in the figures and tables that follow. The marginal stability curves for a fluid layer with $\Delta\sigma/\sigma_0 = 10$ and stress-free boundaries are shown in Figs. 2 and 3. In Fig. 2, Gr_e is plotted versus α at $Sc_e = 10^3$, 10^4 and 10^5. In Fig. 3, these data are re-plotted as Ra_e versus α, and the three curves collapse into one. Thus, as indicated in section IV, the marginal stability curves associated with Eqs. (50)-(52) depend on $\Delta\sigma/\sigma_0$ and $Sc_e Gr_e$ when $\tau \to \infty$. These results are also shown in Table I, where marginal stability values of Ra_e vs. α are listed for $Sc_e = 10^3$, 10^4 and 10^5; Ra_e values agree to four digits across a two decade variation in Sc_e. For $\Delta\sigma/\sigma_0 = 10$ and stress-free boundaries, the critical Ra_e is 1.504×10^4 and the critical wave number is 1.98.

When $\Delta\sigma/\sigma_0$ is increased, the minimum of the marginal stability curve shifts to slightly higher wave numbers (Fig. 4). More importantly, the magnitude of the critical Ra_e increases with $\Delta\sigma/\sigma_0$. This seems counterintuitive inasmuch as the region of stability widens as the conductivity increment of the base state increases. Recall, however, that

$$Ra_e = \frac{\varepsilon E_0^2 d^2}{\mu K_{\text{eff}}} \frac{\Delta\sigma}{\sigma_0}.$$

So, even though the critical Ra_e increases monotonically with $\Delta\sigma/\sigma_0$, the critical electric field strength does not. Plots of $\mathcal{E}^2 \equiv \varepsilon E_0^2 d^2/\mu K_{\text{eff}}$ versus α are shown in Fig. 5; $\mathcal{E}^2$ can be thought of as the square of the dimensionless field strength or, alternatively, as the

scaled electric energy density. Notice that the magnitude of the critical $\mathcal{E}^2$ goes through a minimum as $\Delta\sigma/\sigma_0$ is increased. This again seems to contradict the notion that sharpening the conductivity increment in the base state favors instability. However, it will be seen that the widening of the stability region for $\Delta\sigma/\sigma_0 > 20$ is due to boundary effects.

The imposition of the electric field on the base state conductivity gradient induces within the fluid layer a volume charge, the distribution of which is given by Eq. (31). The base state field acts on the volume charge to produce a coulombic body force that is proportional to $\bar{E}_z\, d\bar{E}_z/dz$. This electrical body force is opposed by the base state pressure gradient. But, for reasons outlined in Section I, this balance of forces is not necessarily stable. When a small fluid parcel is displaced upward (or downward) it is surrounded locally by a fluid of higher (or lower) conductivity. Due to the conductivity differences, a polarization charge, proportional to the local strength of the base state electric field $\bar{E}_z$, is induced about the periphery of the parcel. This polarization charge develops instantaneously compared to the response times of the fluid and the conductivity profile, i.e.

$$\varepsilon/\sigma_0 << d^2/\nu \quad \text{and} \quad d^2/K_{\text{eff}}.$$

The local field gradient acts on the polarization charge much like it would on an induced dipole, exerting a force that is proportional to $\bar{E}_z\, d\bar{E}_z/dz$. This force is similar to that which gives rise to the dielectrophoresis of leaky dielectric drops and tends to perpetuate the motion of the parcel in the direction of its original displacement[9]. If the viscous stresses can resist the motion of the parcel well enough for ionic diffusion to dissipate the local conductivity differences, the motion of the parcel is arrested. If they cannot, the parcel continues on upward (or downward) and instability ensues.

In Fig. 6, the profile of $\overline{E}_z \, d\overline{E}_z/dz$ is plotted for several values of $\Delta\sigma/\sigma_0$. The portion of fluid in which the (destabilizing) dielectrophoretic forces are appreciable is proximal to the lower-conductivity boundary ($z = 0$) and becomes increasingly narrow as $\Delta\sigma/\sigma_0$ increases. Accordingly, at high values of $\Delta\sigma/\sigma_0$, one would expect the lower boundary to exert a strong stabilizing influence, especially in comparison to that of the upper boundary.

Figures 7, 8 and 9 are plots of the marginal stability curves $\mathcal{E}^2$ vs. α at $\Delta\sigma/\sigma_0 = 1000$, 100 and 50, respectively. Results are shown for four kinds of boundary conditions: (1), both boundaries rigid; (2), the upper boundary stress-free and the lower one rigid; (3), the upper boundary rigid and the lower one stress-free; and, (4), both boundaries stress-free. The effect of the conditions imposed at the upper boundary is clearly secondary to that of the conditions imposed at the lower. This is evident in two ways. First, the marginal stability curves of those cases that share a common boundary condition at $z = 0$ are closest. Second, changing the boundary condition at $z = 1$ (e.g. from stress-free to rigid) shifts the marginal stability curves by a factor of 2 or so in $\mathcal{E}^2$, while a change in the condition at $z = 0$ shifts the curves by as much as a factor of 100. It would seem then that the minimum in the variation of $\mathcal{E}^2_{\text{crit}}$ with $\Delta\sigma/\sigma_0$ (Fig. 10) is due to the increasing influence of the lower-conductivity boundary as $\Delta\sigma/\sigma_0$ increases.

Comparison of the foregoing results with experimental observations are favorable but far from definitive. Electrohydrodynamic instabilities were manifested in microgravity IEF experiments[10] performed on aqueous electrolyte buffers at field strengths of approximately $1.7 kV/m$ and current densities of $17 A/m^2$. Numerical simulations of the IEF processes indicate that, were these IEF experiments to have proceed without the onset of convection, conductivity variations exceeding an order of magnitude would occur over distances of about $1 mm$ [11,12,15]. Using the viscosity and dielectric constant of water,

$d = 1mm$, $K_{\text{eff}} = 10^{-10}\, m^2/s$, and a conductivity $\sigma_0 = 10^{-2}\, S/m$, the results for stress-free boundaries and $\Delta\sigma/\sigma_0 = 10$ give a critical field strength $E_{0,\,\text{crit}} = 0.4\, kV/m$ and a critical current density $J_{0,\,\text{crit}} = 4\, A/m^2$. Thus, under experimental conditions for which the predicted critical field strength (or, alternatively the critical current density) was exceeded, instability was indeed observed[10].

Concluding Remarks

This analysis shows that electrically-driven convection can ensue in an initially quiescent fluid layer with an electrical conductivity gradient. The fluid instability is due to dielectrophoretic forces that stem from local electrical conductivity differences in the fluid. If diffusive transport of charge-carrying solutes is sufficiently fast, the dielectrophoretic forces vanish with the relaxation of conductivity differences and quiescence persists in the layer. In this work, the diffusive relaxation of conductivity differences has been lumped into a single parameter K_{eff}, which appears in a convective-diffusion balance on σ.

The implications of the results are that, in order to maintain stability in the fluid layer, the magnitude of the conductivity gradient and electric field must be controlled. The magnitude of $\Delta\sigma/\sigma_0$ dictates the magnitude of the critical field strength that can be imposed across the layer before electrohydrodynamic instability ensues. Moreover, it is shown that the conditions prescribed at the lower-conductivity boundary have a significant effect on the stability of the fluid layer.

References

a) Author to whom correspondence should be addressed.

1 G. I. Taylor and A. D. McEwan, "The stability of a horizontal fluid interface in a vertical electric field," *J. Fluid Mech.*, **22**, 1-15 (1965).

2 D. H. Michael and M. E. O'Neill, "Electrohydrodynamic instability in plane layers of fluid," *J. Fluid Mech.*, **41**, 571-80 (1969).

3 P. H. Rhodes, R. S. Snyder, G. O. Roberts, "Electrohydrodynamic distortion of sample streams in continuous flow electrophoresis," *J. Colloid Interface Sci.*, **129**, 78 (1989).

4 J. R. Melcher and G. I. Taylor, "Electrohydrodynamics: a review of the role of interfacial shear stresses," *Ann. Rev. Fluid Mech.*, **1**, 111-46 (1969).

5 R. J. Turnbull and J. R. Melcher, "Electrohydrodynamic Rayleigh-Taylor instability," *Phys. Fluids*, **12**, 1160-66 (1969).

6 J. R. Melcher and M. S. Firebaugh, "Traveling-wave bulk electroconvection induced across a temperature gradient," *Phys. Fluids*, **10**, 1178-85 (1967).

7 J. F. Hoburg and J. R. Melcher, "Electrohydrodynamic mixing and instability induced by colinear fields and conductivity gradients," *Phys. Fluids*, **20**, 903-911 (1977).

8 J. F. Hoburg, "Internal electrohydrodynamic instability of liquids with colinear fields and conductivity gradients," *J. Fluid Mech.*, **84**, 291-303 (1978).

9 J. C. Baygents, "The electrohydrodynamics of drop dielectrophoresis," *J. Fluid Mech.*, submitted, 1994.

10 M. Bier, "Isoelectric focusing in space and spinoffs," in *AIAA/IKI Microgravity Science Symposium*, edited by F.J. Kohl (AIAA, Washinton, DC, 1990), pp. 221-227.

Table I

Marginal Stability Values for Ra_e versus α and Sc_e at $\Delta\sigma/\sigma_0 = 10$.

α	Ra_e @ $Sc_e = 10^3$	Ra_e @ $Sc_e = 10^4$	Ra_e @ $Sc_e = 10^5$
1.0	25460	25460	25463
1.1	22512	22511	22508
1.2	20339	20339	20344
1.3	18721	18721	18718
1.4	17513	17513	17510
1.5	16618	16617	16619
1.6	15967	15968	15971
1.7	15515	15514	15510
1.8	15226	15226	15224
1.9	15077	15076	15081
2.0	15048	15049	15048
2.1	15128	15129	15125
2.2	15308	15307	15312
2.3	15579	15579	15576
2.4	15939	15939	15938
2.5	16385	16385	16389

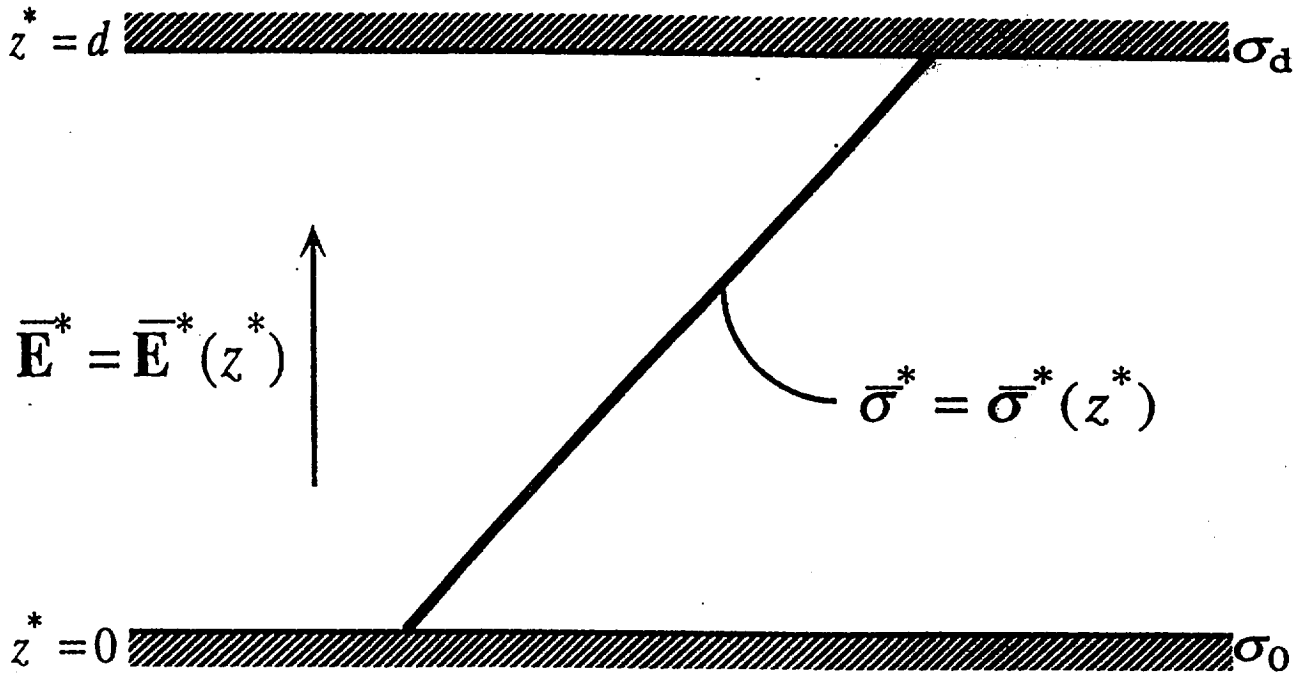

Fig. 1 An initially quiescent and steady fluid layer of infinite extent in the x and y directions with a linear electrical conductivity gradient in the z direction. Asterisks are affixed to the variables to indicate that they are in dimensional form; cf. Eq. (13).

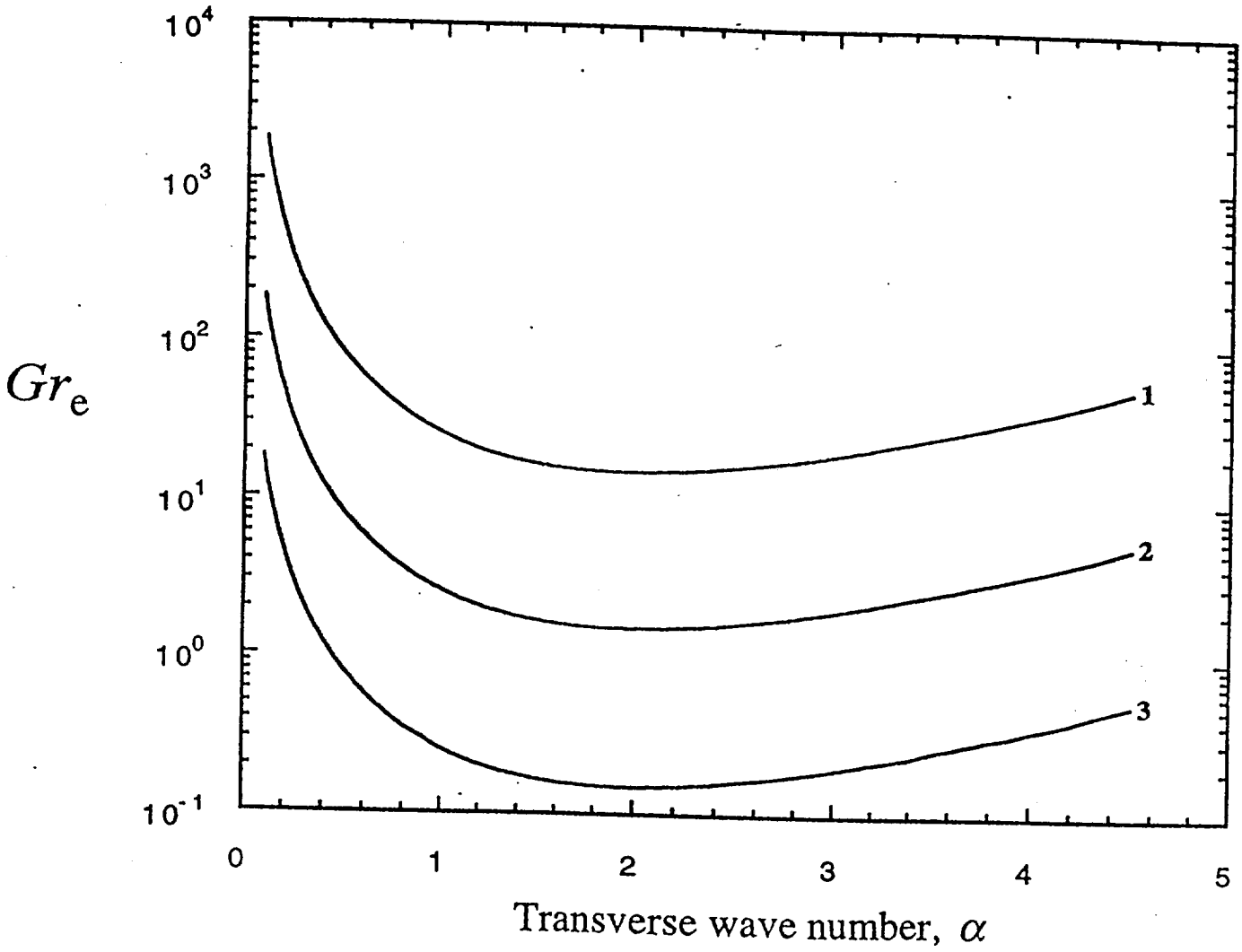

Fig. 2 Neutral stability curves for stress-free boundary conditions; $\Delta\sigma/\sigma_0 = 10$; $\tau = 10^8$. Legend: **1.** $Sc_e = 10^3$, $Gr_{e,\,crit} = 15.04$, $\alpha_{crit} = 1.98$; **2.** $Sc_e = 10^4$, $Gr_{e,\,crit} = 1.504$, $\alpha_{crit} = 1.98$; **3.** $Sc_e = 10^5$, $Gr_{e,\,crit} = 0.1504$, $\alpha_{crit} = 1.98$.

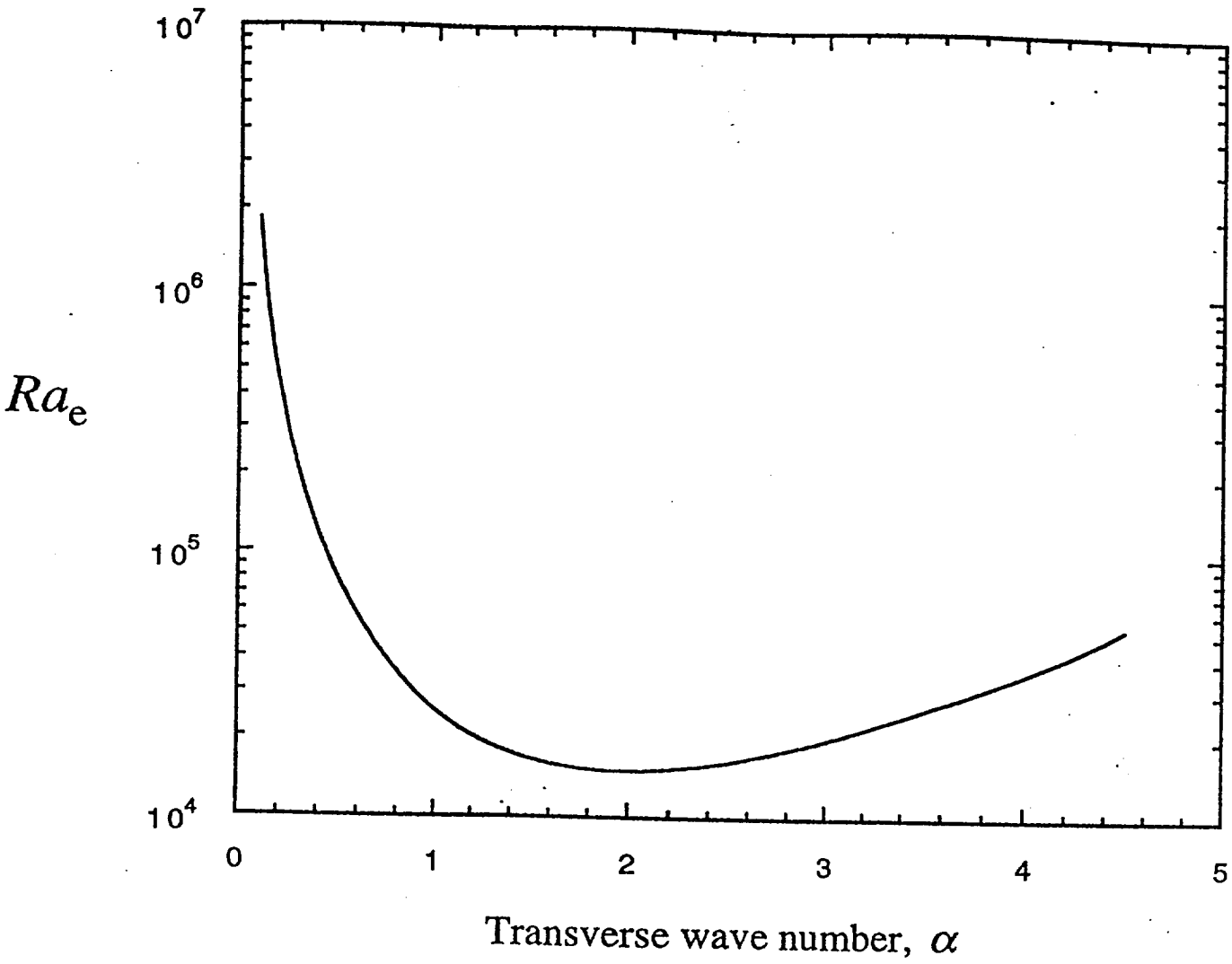

Fig. 3 Neutral stability curves for stress-free boundary conditions; $\Delta\sigma/\sigma_0 = 10$; $\tau = 10^8$. The critical Ra_e and α are 1.504×10^4 and 1.98 respectively.

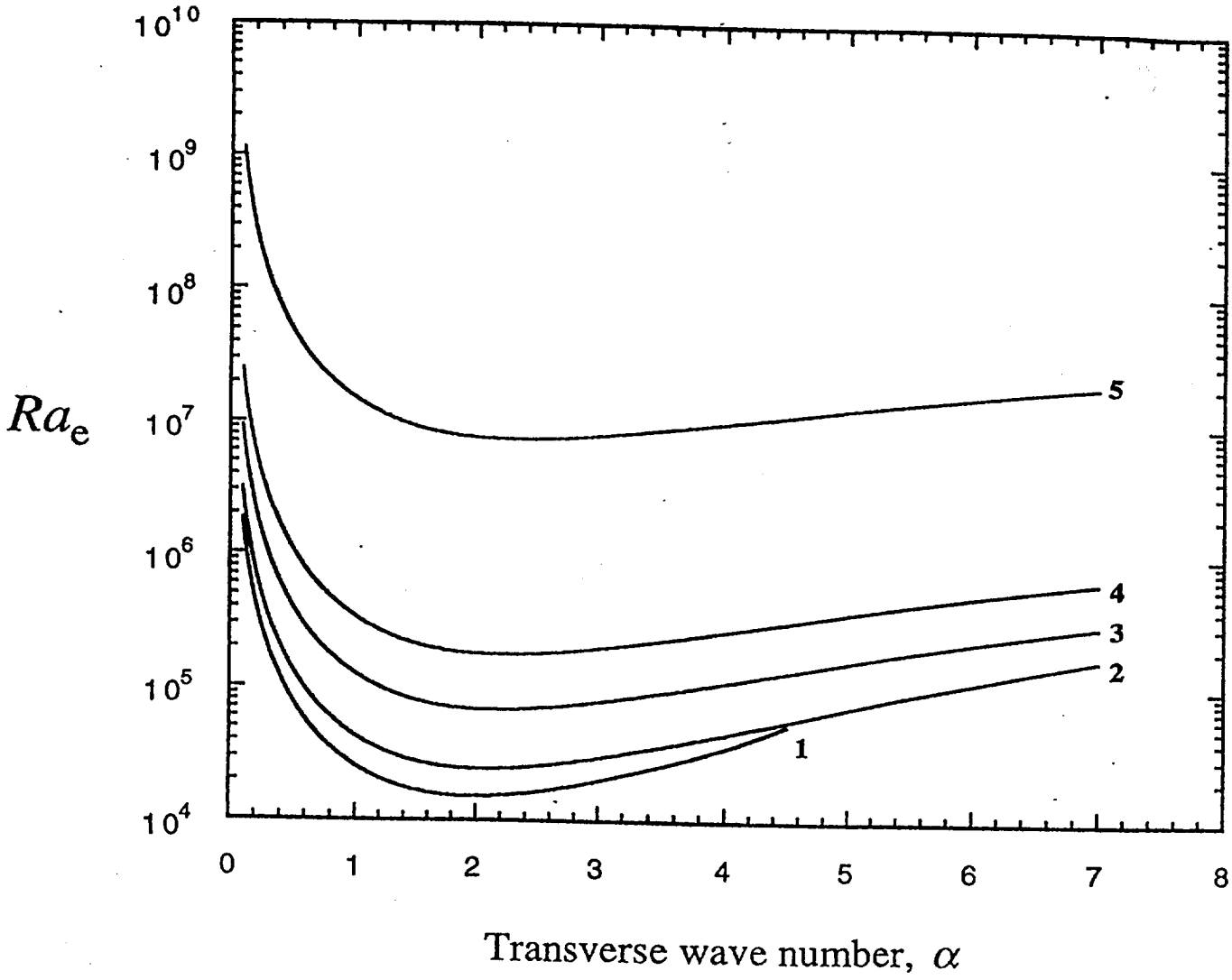

Fig. 4 Neutral stability curves for the stress-free boundary conditions; $\tau = 10^8$. Legend: **1**. $\Delta\sigma/\sigma_0 = 10$, $Ra_{e,\,crit} = 1.504 \times 10^4$, $\alpha_{crit} = 1.98$; **2**. $\Delta\sigma/\sigma_0 = 20$, $Ra_{e,\,crit} = 2.430 \times 10^4$, $\alpha_{crit} = 2.06$; **3**. $\Delta\sigma/\sigma_0 = 50$, $Ra_{e,\,crit} = 6.788 \times 10^4$, $\alpha_{crit} = 2.16$; **4**. $\Delta\sigma/\sigma_0 = 100$, $Ra_{e,\,crit} = 1.766 \times 10^5$, $\alpha_{crit} = 2.22$; **5**. $\Delta\sigma/\sigma_0 = 1000$, $Ra_{e,\,crit} = 7.407 \times 10^6$, $\alpha_{crit} = 2.34$.

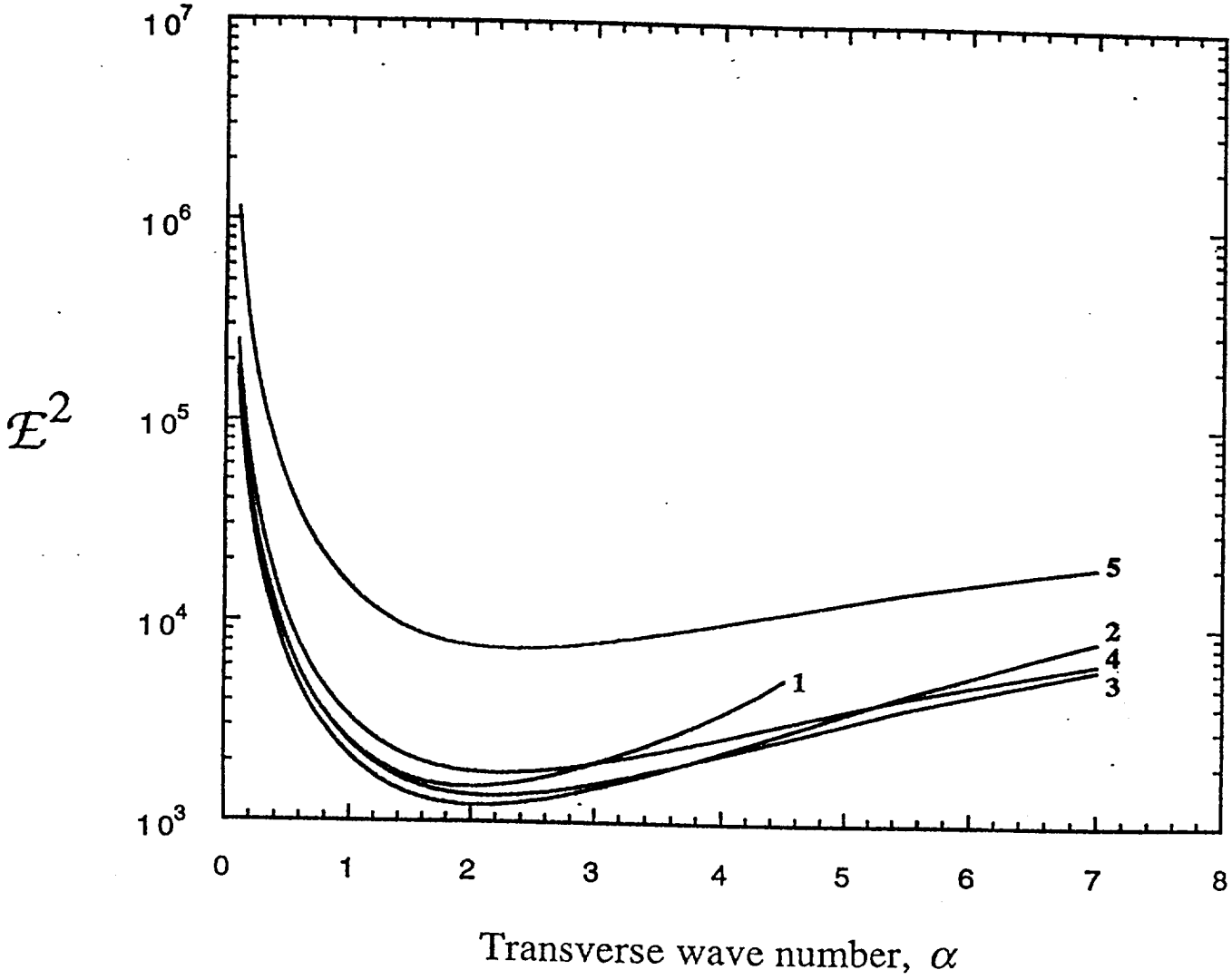

Fig. 5 Neutral stability curves for the stress-free boundary conditions; $\tau = 10^8$. Legend: **1**. $\Delta\sigma/\sigma_0 = 10$, $\mathcal{E}^2_{crit} = 1.505 \times 10^3$, $\alpha_{crit} = 1.98$; **2**. $\Delta\sigma/\sigma_0 = 20$, $\mathcal{E}^2_{crit} = 1.215 \times 10^3$, $\alpha_{crit} = 2.06$; **3**. $\Delta\sigma/\sigma_0 = 50$, $\mathcal{E}^2_{crit} = 1.358 \times 10^3$, $\alpha_{crit} = 2.16$; **4**. $\Delta\sigma/\sigma_0 = 100$, $\mathcal{E}^2_{crit} = 1.766 \times 10^3$, $\alpha_{crit} = 2.22$; **5**. $\Delta\sigma/\sigma_0 = 1000$, $\mathcal{E}^2_{crit} = 7.407 \times 10^3$, $\alpha_{crit} = 2.34$.

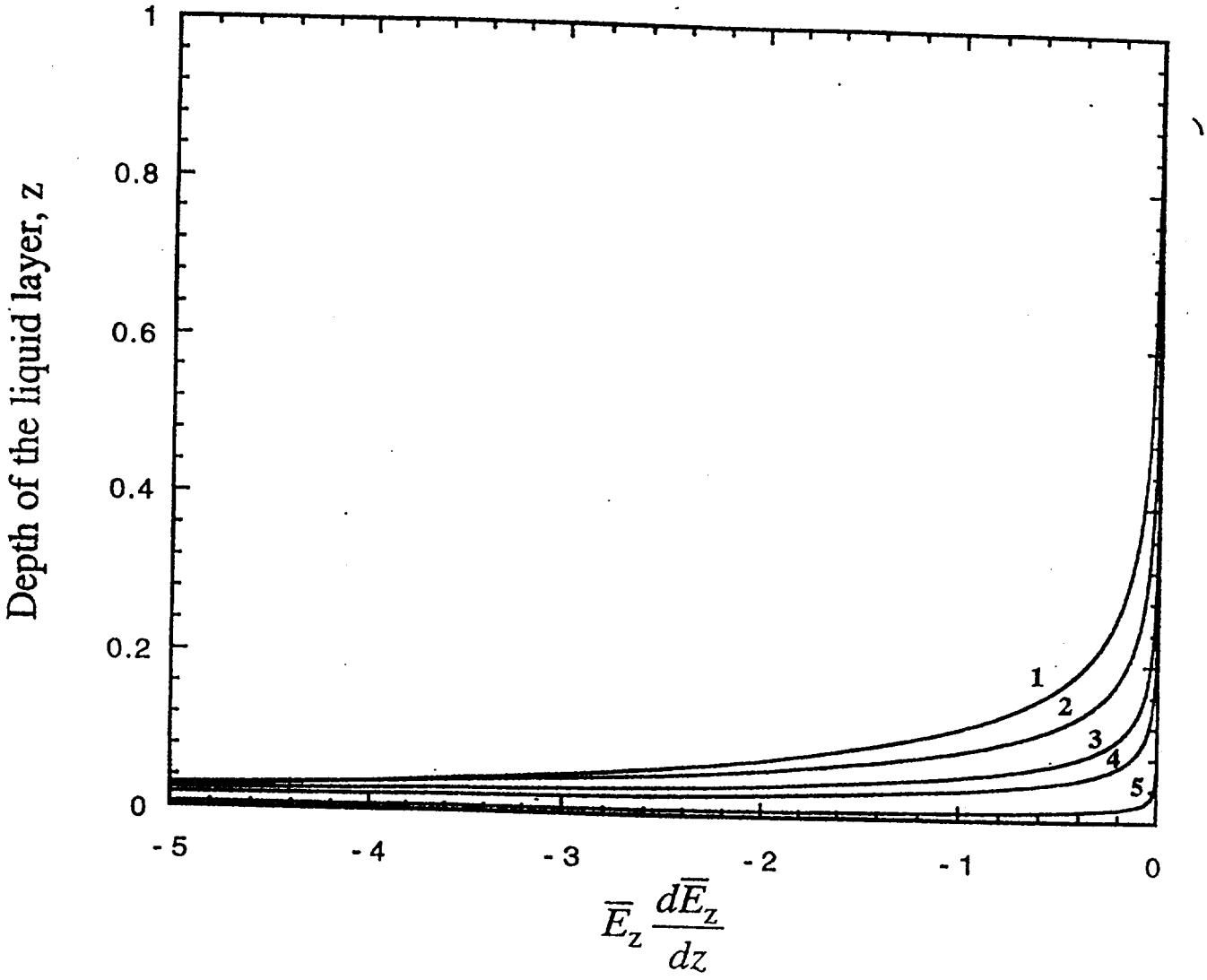

Fig. 6 The profile of $\overline{E}_z\, d\overline{E}_z/dz$ across the liquid layer for several values of $\Delta\sigma/\sigma_0$. Legend: **1**. $\Delta\sigma/\sigma_0 = 10$; **2**. $\Delta\sigma/\sigma_0 = 20$; **3**. $\Delta\sigma/\sigma_0 = 50$; **4**. $\Delta\sigma/\sigma_0 = 100$; **5**. $\Delta\sigma/\sigma_0 = 1000$.

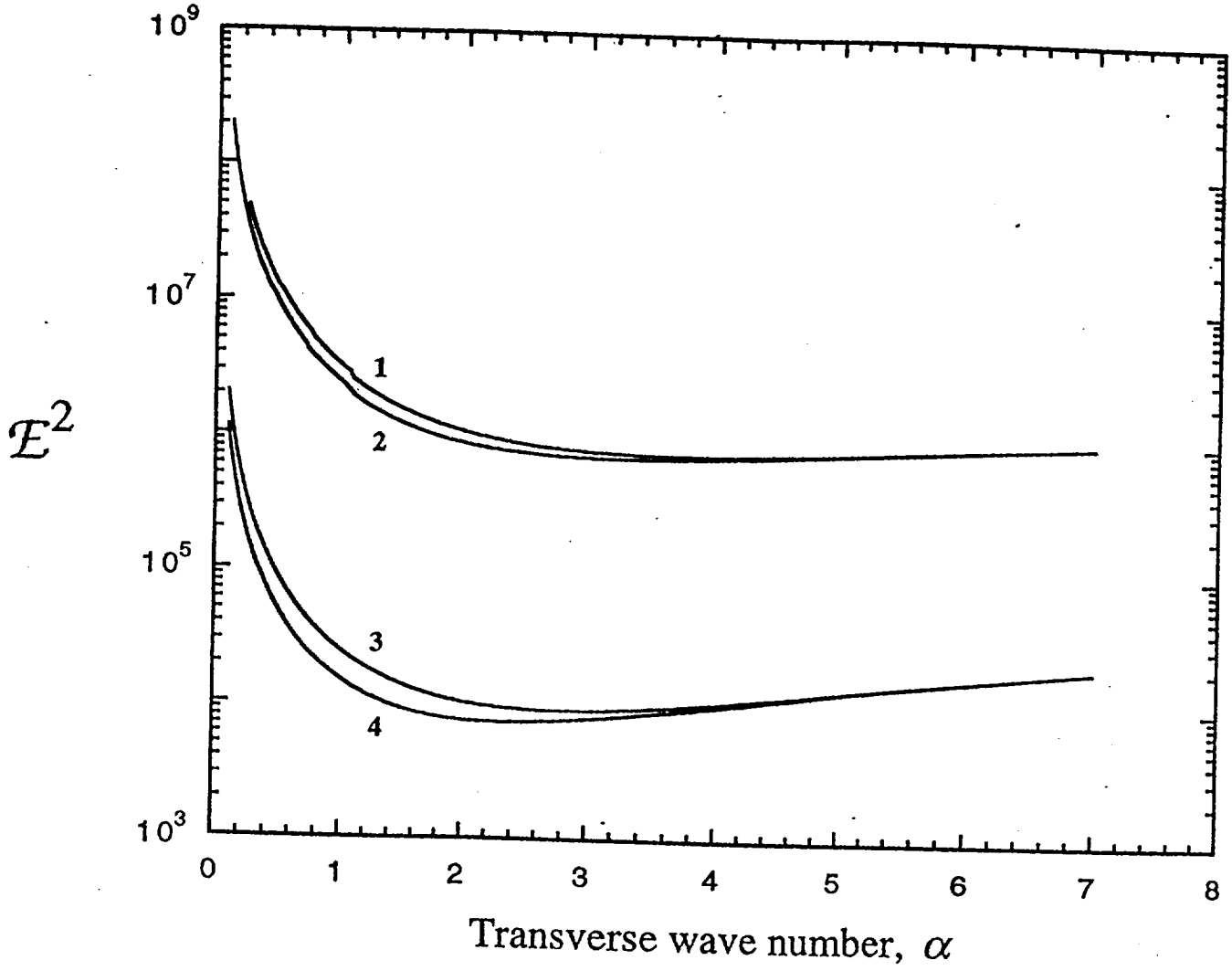

Fig. 7 Neutral stability curves for $\Delta\sigma/\sigma_0 = 1000$ for the four kinds of boundary conditions. Legend: **1.** rigid-boundaries; **2.** the upper boundary stress-free and the lower one rigid; **3.** the upper boundary rigid and the lower one stress-free; **4.** stress-free boundaries. For all these curves $\tau = 10^8$.

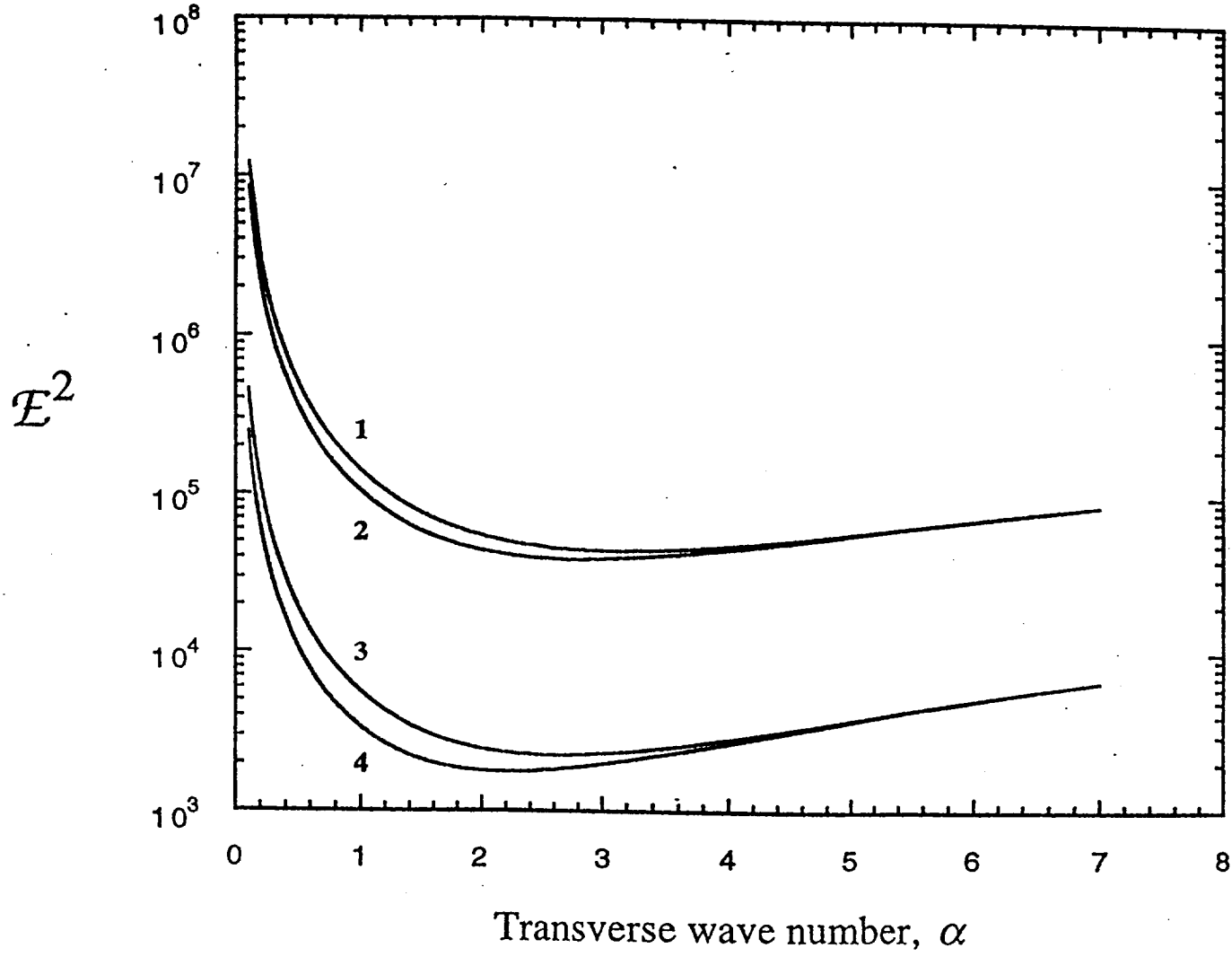

Fig. 8 Neutral stability curves for $\Delta\sigma/\sigma_0 = 100$ for the four kinds of boundary conditions. Legend: **1.** rigid-boundaries; **2.** the upper boundary stress-free and the lower one rigid; **3.** the upper boundary rigid and the lower one stress-free; **4.** stress-free boundaries. For all these curves $\tau = 10^8$.

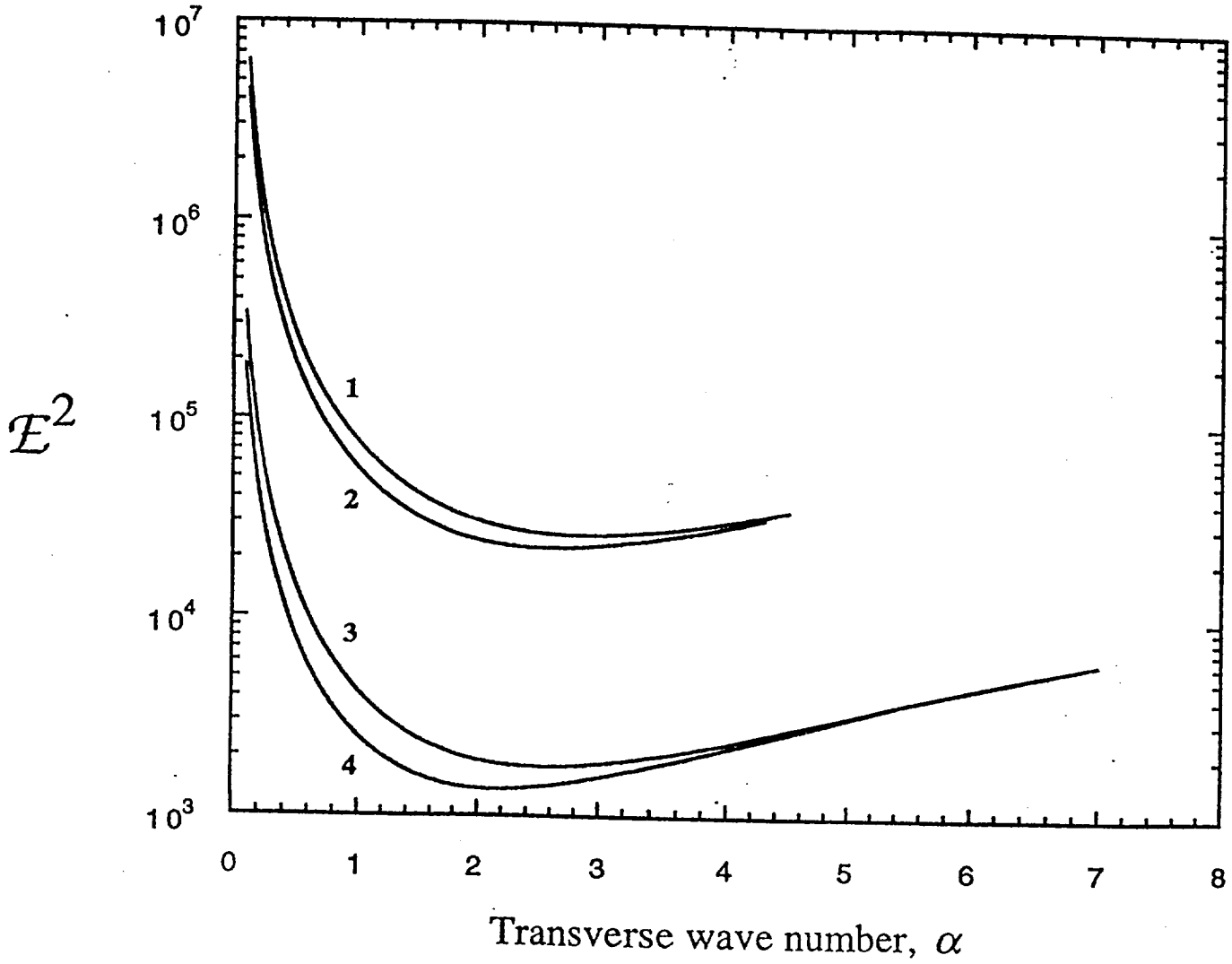

Fig. 9 Neutral stability curves for $\Delta\sigma/\sigma_0 = 50$ for the four kinds of boundary conditions. Legend: **1.** rigid-boundaries; **2.** the upper boundary stress-free and the lower one rigid; **3.** the upper boundary rigid and the lower one stress-free; **4.** stress-free boundaries. For all these curves $\tau = 10^8$.

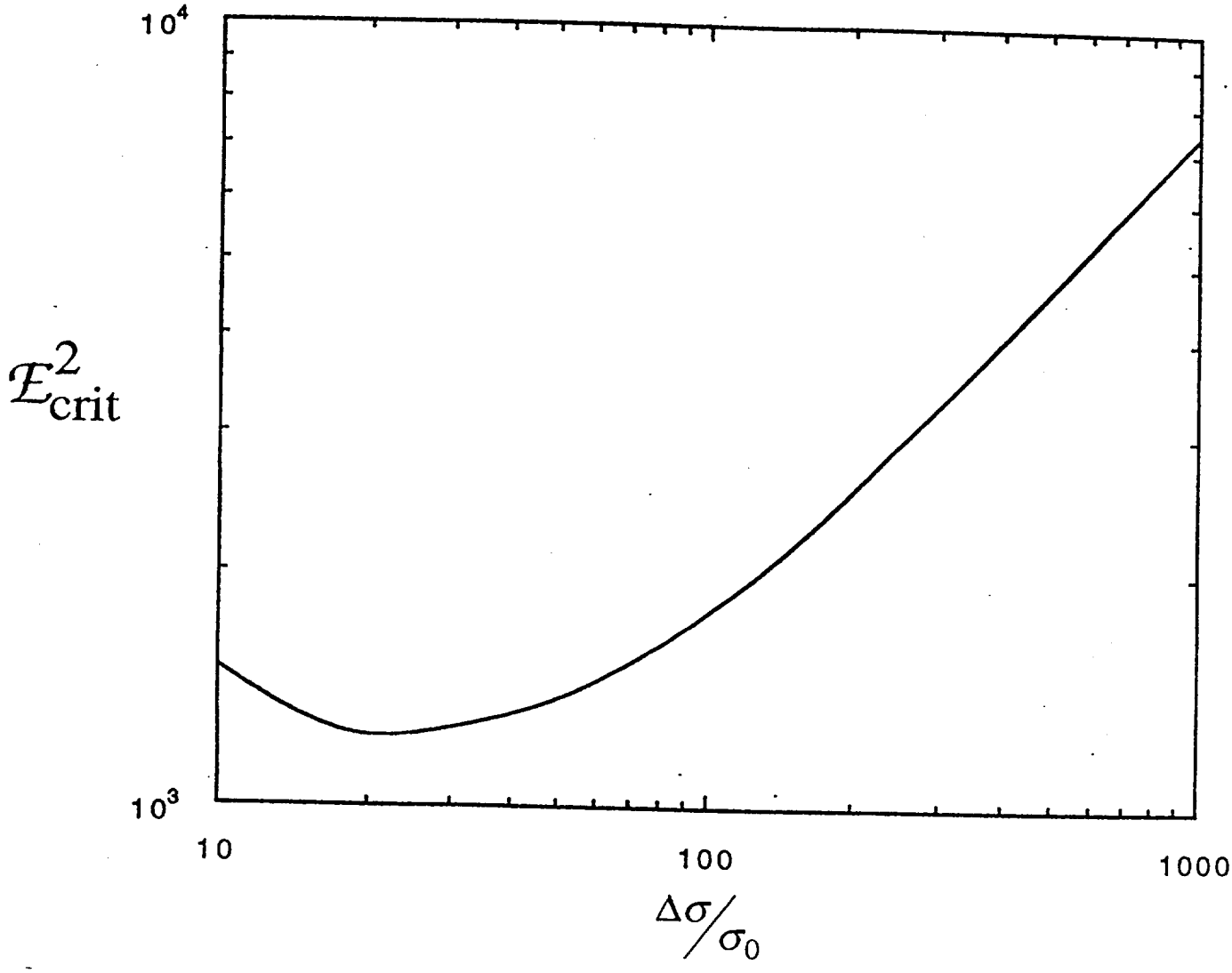

Fig. 10 The variation of $\mathcal{E}^2_{crit}$ with $\Delta\sigma/\sigma_0$ for stress-free boundaries.

APPENDIX 1 : AN ESTIMATE OF THE CONDUCTIVITY GRADIENTS REQUIRED TO PRODUCE THE CONVECTION OBSERVED IN IEF SPACE-FLIGHT EXPERIMENTS

To obtain an estimate of the magnitude of the conductivity gradients needed to yield the flow strengths observed during the (STS-11 and STS-26) microgravity experiments, a scale analysis of the momentum balance is performed as follows. The Reynolds number is a measure of the relative magnitude of inertial and viscous effects, and it is defined as

$$\mathrm{Re} \equiv \frac{\text{inertial}}{\text{viscous}} = \frac{\rho\left(U^c\right)^2 / l^c}{\mu U^c / \left(l^c\right)^2} = \frac{U^c l^c}{\mu/\rho} = \frac{U^c l^c}{\nu}. \qquad (1)$$

For the present analysis, the focusing chamber is assumed to have cylindrical geometry, and from experimental results, the flows encountered have a velocity on the order of 1 cm/min, in a capillary of 0.5 cm diameter. The kinematic viscosity of the buffer solution is approximately that of water at room temperature, $10^{-6} m^2 s^{-1}$. Thus,

$$\mathrm{Re} \sim \frac{(10^{-2}\, m/\mathrm{min})(5\times 10^{-3} m)(\frac{1}{60}\,\mathrm{min}/s)}{10^{-6}\, m^2/s} = 0.8 \sim 1, \qquad (2)$$

which indicates that the inertial and viscous effects are of comparable magnitude.

To asses the significance of the electrical effects, they are compared to the viscous effects, since the momentum generated by electrical stresses is transferred at the onset of motion by viscous action. From the Navier-Stokes equations, a balance of the viscous and electrical terms requires

$$\mu\nabla^2\mathbf{v} - \nabla p \approx \frac{1}{2}\mathbf{E}\cdot\mathbf{E}\nabla\varepsilon - \rho_f\mathbf{E} \tag{3}$$

where $\approx$ is understood to mean that the terms are of similar magnitude. Substituting Eqs. (8) and (11) from chapter 2 into (3) above, one finds

$$\mu\nabla^2\mathbf{v} - \nabla p \approx \frac{1}{2}\mathbf{E}\cdot\mathbf{E}\,\nabla\varepsilon - \left[\frac{\varepsilon}{\sigma}\mathbf{v}\cdot\nabla(\nabla\varepsilon\cdot\mathbf{E} + \varepsilon\nabla\cdot\mathbf{E}) + \left(\nabla\varepsilon - \varepsilon\frac{\nabla\sigma}{\sigma}\right)\cdot\mathbf{E}\right]\mathbf{E}. \tag{4}$$

Since for IEF the gradient in the dielectric constant is negligible,

$$\mu\nabla^2\mathbf{v} - \nabla p \approx \left[\frac{\varepsilon}{\sigma}\mathbf{v}\cdot\nabla(\varepsilon\nabla\cdot\mathbf{E}) - \varepsilon\frac{\nabla\sigma}{\sigma}\cdot\mathbf{E}\right]\mathbf{E}. \tag{5}$$

Also

$$\nabla(\varepsilon\nabla\cdot\mathbf{E}) = \nabla\varepsilon(\nabla\cdot\mathbf{E}) + \varepsilon\nabla(\nabla\cdot\mathbf{E}) \cong \varepsilon\nabla(\nabla\cdot\mathbf{E}), \tag{6}$$

which leaves

$$\mu\nabla^2\mathbf{v} - \nabla p \approx \left[\frac{\varepsilon^2}{\sigma}\mathbf{v}\cdot\nabla(\nabla\cdot\mathbf{E}) - \varepsilon\frac{\nabla\sigma}{\sigma}\cdot\mathbf{E}\right]\mathbf{E}. \tag{7}$$

From Eq. (7), it follows that

$$\varepsilon \frac{\nabla\sigma}{\sigma} E_c^2 \sim \mu \frac{U_c}{l_c^2} + \frac{\varepsilon^2}{\sigma} U_c \frac{E_c^2}{l_c^2} \tag{8}$$

or

$$\frac{\nabla\sigma}{\sigma} \sim \mu \frac{U_c}{l_c^2} \frac{1}{\varepsilon E_c^2} + \frac{\varepsilon}{\sigma} \frac{U_c}{l_c^2}. \tag{9}$$

For the IEF experiments $\mu\sigma/(\varepsilon E_c)^2 >> 1$, so

$$\frac{\nabla\sigma}{\sigma} \sim \frac{(10^{-3}\, kg/(m\times s))(10^{-2}\, m/\min)(\frac{1}{60}\min/s)}{(80)(8.854\times 10^{-12}\, C/(V\times m))(1667\, V/m)^2(5\times 10^{-3} m)^2} \cong 3\ m^{-1}. \tag{10}$$

Equation (10) indicates that $\nabla\sigma/\sigma$ need only be *ca.* 3 m^{-1} to produce flows of strength 1 cm/min in the IEF flight experiments. The simulation results shown n Fig. 21 of Chapter 1 indicate that gradients of this magnitude are realizable in IEF.

APPENDIX 2 : THE CHARGE CONSERVATION AND CONDUCTIVITY EVOLUTION EQUATIONS

Conservation of Charge

In systems where conduction involves more than one charged species (e.g. aqueous electrolytes), each of the charges is governed by a conservation equation

$$\frac{\partial \rho_{\pm}}{\partial t} + \nabla \cdot (\rho_{\pm} \mathbf{v} \pm \mathbf{J}_{\pm}) = 0, \tag{1}$$

where the current density for a bipolar conductor is

$$\mathbf{J}_{\pm} = b_{\pm} \rho_{\pm} \mathbf{E} \mp K_{\pm} \nabla \rho_{\pm}, \tag{2}$$

Here $b_{\pm}$ are the mobilities and $K_{\pm}$ the diffusivities of the cation (+) and anion (-). The net free charge density and conductivity are

$$\rho_f = \rho_+ - \rho_- \;\; ; \;\; \sigma = b_+ \rho_+ + b_- \rho_-, \tag{3}$$

and

$$\rho_{\pm} = \frac{\sigma \pm b_{\mp} \rho_f}{b_+ + b_-} \tag{4}$$

Substitution of Eqs. (2) and (3) into Eq. (1) and introducing Gauss' law, viz.